NeuroImage 303 (2024) 120914

Contents lists available at ScienceDirect

NeuroImage

journal homepage: www.elsevier.com/locate/ynimg

Decoding cortical chronotopy—Comparing the influence of different cortical organizational schemes

Falko Mecklenbrauck [a,b,*], Jorge Sepulcre [c], Jana Fehring [b,d], Ricarda I. Schubotz [a,b]

[a] Department of Psychology, Biological Psychology, University of Münster, Germany
[b] Otto Creutzfeldt Center for Cognitive and Behavioral Neuroscience, University of Münster, Germany
[c] Department of Radiology and Biomedical Imaging, Yale PET Center, Yale School of Medicine, Yale University, New Haven, CT, USA
[d] Institute for Biomagnetism and Biosignal Analysis, Münster, Germany

ARTICLE INFO

Keywords:
Bayesian model comparison
Cortical timescales
DWI
fMRI
Nested hierarchies
Inter-subject correlation
Cortical hierarchies

ABSTRACT

The brain's diverse intrinsic timescales enable us to perceive stimuli with varying temporal persistency. This study aimed to uncover the cortical organizational schemes underlying these variations, revealing the neural architecture for processing a wide range of sensory experiences. We collected resting-state fMRI, task-fMRI, and diffusion-weighted imaging data from 47 individuals. Based on this data, we extracted six organizational schemes: (1) the structural Rich Club (RC) architecture, shown to synchronize the connectome; (2) the structural Diverse Club architecture, as an alternative to the RC based on the network's module structure; (3) the functional uni-to-multimodal gradient, reflected in a wide range of structural and functional features; and (4) the spatial posterior/lateral-to-anterior/medial gradient, established for hierarchical levels of cognitive control. Also, we explored the effects of (5) structural graph theoretical measures of centrality and (6) cytoarchitectural differences. Using Bayesian model comparison, we contrasted the impact of these organizational schemes on (1) intrinsic resting-state timescales and (2) inter-subject correlation (ISC) from a task involving hierarchically nested digit sequences. As expected, resting-state timescales were slower in structural network hubs, hierarchically higher areas defined by the functional and spatial gradients, and thicker cortical regions. ISC analysis demonstrated hints for the engagement of higher cortical areas with more temporally persistent stimuli. Finally, the model comparison identified the uni-to-multimodal gradient as the best organizational scheme for explaining the chronotopy in both task and rest. Future research should explore the microarchitectural features that shape this gradient, elucidating how our brain adapts and evolves across different modes of processing.

1. Introduction

The discovery that different brain regions vary in terms of their processing rhythms or *intrinsic timescales* (Murray et al., 2014; Ogawa and Komatsu, 2010; Raut et al., 2020) sparked the investigation of the possible function of these timescales (for reviews see Cavanagh et al., 2020; Soltani et al., 2021). One exciting idea is that cortical processes are organized according to a hierarchy of timescales (Chen et al., 2015; Hasson et al., 2015; Jeon, 2014; Manea et al., 2022). The different intrinsic timescales make our brain perfectly adapted for the processing and representation of the different external nested rhythms in nature (Golesorkhi et al., 2021b; Wolff et al., 2022). Thus, different areas of the brain can segregate and integrate incoming stimuli depending on their own intrinsic timescale and the temporal structure of the stimulus (Baldassano et al., 2017; Cavanagh et al., 2020; Golesorkhi et al., 2021b).

Using hierarchically nested stimuli, previous studies were able to distinguish cortical areas according to their specific response to hierarchical levels of temporally persistency of the stimulus (Aberbach-Goodman and Mukamel, 2023; Farbood et al., 2015; Hasson et al., 2008; Lerner et al., 2011). For each region, a so-called *temporal receptive window* (TRW) was determined (Hasson et al., 2008). Analogical to spatial receptive windows, TRWs describe the specific time frame of an area in which information of the ongoing stimulus is integrated (Hasson et al., 2015). Appropriately, areas with longer TRWs were also found to have slower intrinsic timescales (Chaudhuri et al., 2015; Gao

---

* Corresponding author at: University of Münster, Institute of Psychology, Fliednerstr. 21, D-48149 Münster, Germany.

E-mail addresses: f_meck01@uni-muenster.de (F. Mecklenbrauck), jorge.sepulcre@yale.edu (J. Sepulcre), fehringj@uni-muenster.de (J. Fehring), rschubotz@uni-muenster.de (R.I. Schubotz).

https://doi.org/10.1016/j.neuroimage.2024.120914
Received 15 July 2024; Received in revised form 22 October 2024; Accepted 1 November 2024

et al., 2020; Honey et al., 2012; Moraczewski et al., 2020; Stephens et al., 2013).

The origin of different intrinsic cortical timescales and TRWs however has yet to be determined. The current paper aims to explore and evaluate multiple alternative cortical foundations of this *chronotopy*. To this end, we compared the congruity of different, established cortical organizational schemes with the chronotopy of the cortex at rest and during a task.

For the chronotopy at rest, we collected resting-state functional magnetic resonance imaging (rs-fMRI) and applied a model-free approach (Raut et al., 2020) to calculate the autocorrelation decay of each area, which is a valid and direct measure to estimate the intrinsic cortical timescales (Zilio et al., 2021). The variance of timescales contains meaningful information to distinguish between different cortical areas (Murray et al., 2014; Ogawa and Komatsu, 2010).

To investigate the chronotopy in a task-setting, we used hierarchically nested stimuli to ascertain the distribution of TRWs across the cortex. Based on previous TRW studies (Farbood et al., 2015; Hasson et al., 2008; Lerner et al., 2011), we designed digit sequences of four different, nested levels of temporal persistency. We used inter-subject correlation (ISC; Hasson et al., 2004, 2010) to determine the reliability of the cortical signal for the four hierarchically structured levels of the stimulus and thus identified areas that integrate information over shorter or longer periods of time.

Regarding potential cortical foundations of the chronotopy, we considered in total six commonly reported organizational schemes and features:

(1) The structural Rich Club (RC) is a set of highly interconnected network nodes (Colizza et al., 2006), topologically organized in resonant network motifs that are particularly efficient in synchronizing neighbouring nodes via their slow intrinsic timescales (Aguilar-Velázquez and Guzmán-Vargas, 2019; Gollo et al., 2015; Gómez-Gardeñes et al., 2010; Senden et al., 2017; Watanabe, 2013). This finding was recently supported by studies showing that the intrinsic cortical timescales correlate with the connectivity of a node (Fallon et al., 2020; Lurie et al., 2024; Sethi et al., 2017). Due to its particular architecture of connections, the RC organization was previously proclaimed as the prime candidate to shape the brain's diverse temporal dynamics (Gollo et al., 2015; Zamora-López et al., 2016).

(2) The structural Diverse Club (DC) was discussed as a competing topological concept to the RC and possibly might be even more meaningful for the communication of the network (Bertolero et al., 2017). Instead of the nodal degree the DC is based on the structural participation coefficient which describes the membership of a node to multiple network modules (Guimerà and Nunes Amaral, 2005) and recently was found to relate to the cortical timescales as well (Lurie et al., 2024).

(3) Prior studies on the temporal organization of the brain made a distinction between unimodal and multimodal cortices, finding timescales to be faster in unimodal as compared to multimodal cortical areas (Golesorkhi et al., 2021a; Ito et al., 2020; Shafiei et al., 2020; Wolff et al., 2022). This gradient of cortical hierarchy was also reflected in functional connectivity (Margulies et al., 2016), electrophysiological responses (Gao et al., 2020; Honey et al., 2012), cortical thickness (Burt et al., 2018; Wagstyl et al., 2015), neural development (Sydnor et al., 2021, 2023), and brain evolution (Xu et al., 2020). Also, the topological distribution of TRWs follows a progression from sensory to higher order areas, with the longest TRWs in frontal and parietal association cortices (Hasson et al., 2015; Jääskeläinen et al., 2021). We defined this gradient in two different ways: data-driven, based on the stepwise functional connectivity (Sepulcre et al., 2012) and atlas-based using the previously introduced functional differentiation (Ito et al., 2020) in the atlas by Ji et al. (2019).

(4) Cortical frequencies were furthermore found to progress along a posterior-to-anterior gradient, with the slowest frequencies being detected towards the frontal cortex (Mahjoory et al., 2020). This gradient is part of many classical theories of cognitive control (Fuster, 2001; Kiebel et al., 2008; Koechlin and Summerfield, 2007). Moreover, it was reflected in the expression of genes (Hansen et al., 2021; Hawrylycz et al., 2012) as well as the covariance of cortical thickness (Valk et al., 2020) and correlated with the degree of myelinisation, the brain's metabolism and certain frequencies of the electrophysiological power spectrum (Markello et al., 2022). Lately, the posterior-to-anterior trend was extended by a lateral-to-medial aspect (Alexander and Brown, 2018) forming a posterior/lateral-to-anterior/medial gradient that is also mirrored in the intrinsic cortical dynamics (Mahjoory et al., 2020).

(5) Additionally, we explored how of measures of structural network centrality relate to the cortical chronotopy. These graph theoretical measures classify nodes that are important for an intact communication throughout the network (Hagmann et al., 2008) and were recently found to relate the cortical timescales as well (Fallon et al., 2020; Lurie et al., 2024; Sethi et al., 2017).

(6) Lastly, studies have suggested that an interaction between microstructural and macro-level connectivity patterns affect the temporal layout of the cortex (Huntenburg et al., 2018). More specifically, cytoarchitectonic differences between areas may shape intrinsic timescales at the microscale (Gao et al., 2020), reflecting a relationship between myelinisation and timescales (Ito et al., 2020). Consequently, we also considered cortical thickness, which can approximate microstructural differences (Wagstyl et al., 2015).

We modelled the distribution of intrinsic timescales as well as ISC values across these different, commonly found organizational schemes and comprehensively contrasted their significance using Bayesian model comparison (Vehtari et al., 2017). It has to be noted, that the aforementioned organizational schemes and features of the cortex are not independent of each other (Burt et al., 2018; van den Heuvel et al., 2015; van den Heuvel and Sporns, 2013b). By directly comparing the organizational schemes, this paper seeks to find the model that best explains the emergence of different intrinsic timescales and TRWs across the brain and thus resembles the true cortical organization the closest.

2. Materials & methods

The following method section is divided into five segments: firstly, general information on the data acquisition and first processing steps; secondly, a section on the resting-state data, including preprocessing and the estimation of the intrinsic timescales using autocorrelation decay; thirdly, an explanation of the preprocessing of the task data and calculation of the ISC values; fourthly, we describe the identification of the six organizational schemes of interest, whose influence on the cortical chronotropy we compared; and lastly, we outline all conducted statistical analyses and tests.

2.1. General methods

2.1.1. Participants

Data of 47 participants was collected for this study. One participant was excluded due to movement during the rs-fMRI measurement that exceeded 1.5 times the voxel size. The remaining $N_{RS} = 46$ (32 female, $M = 21.76$, $SD = 2.75$ years, range = 18–28 years) were all right-handed ($M = 85.15$, SD = 16.46; range = 30–100) as assessed by the Edinburgh Handedness Inventory (Oldfield, 1971) and had (corrected-to-) normal vision. Additionally to the analysis of rs-fMRI data and their intrinsic timescales, we also collected task data of the same participants. The task-data was analyzed before using a classic contrast-based fMRI analysis (Mecklenbrauck et al., 2024). The present paper reanalyzed the data using ISC (Hasson et al., 2004, 2010). From the task-fMRI data we had to exclude a further seven participants because of movement during the task session (three participants), sub-par attention to the task (one) and technical difficulties (three). So, the data of $N_{\text{ISC}} = 39$ participants (29 female, $M = 21.67$, $SD = 2.77$ years, range = 18–28) entered the ISC analysis. None reported any history of neurological or psychiatric diseases or any ferromagnetic material inside their bodies. The participants received money or course credit as renumeration on completion of the experiment.

2.1.2. *Procedure and stimuli*

The task-fMRI and the rs-fMRI together with the diffusion-weighted imaging (DWI) data were acquired in two sessions on separate days (Fig. 1). The order of the two session was counterbalanced across participants with $M_{\text{RS}} = 7.02$ days ($SD_{\text{RS}} = 5.93$ days) or $M_{\text{ISC}} = 6.73$ days ($SD_{\text{ISC}} = 4.70$ days) passing between sessions, respectively.

Starting with the DWI-Rest Day, the MRI measurements included an anatomical T1-weighted image (5 min), multiple sequences for DWI (15 min) and rs-fMRI (8 min). The participants were instructed to lie as still as possible during the anatomical and DW imaging but could leave their eyes opened or closed. The experimenters informed the participants via an intercom system about the start of the rs-fMRI measurement during which participants looked at a fixation cross (Agcaoglu et al., 2019; Patriat et al., 2013; Van Dijk et al., 2010). In total 480 rs-fMRI volumes were acquired.

In the scanning session on the fMRI-Task Day participants completed a task presenting them with sequences of digits. A detailed description of the stimuli and their creation was reported before (Mecklenbrauck et al., 2024). To summarize, we created abstract stimuli (hierarchically nested sequences of digits) that were inspired by the structure of the hierarchically nested natural stimuli previously used to identify TRW (e.g., Lerner et al., 2011). The sequences were made up from the digits 4 through 9. Digits 1 to 3 were excluded due to their representation as quantities (Dehaene, 2001). The sequences were presented one digit at a time. The hierarchically nested structure of the sequences created four experimental conditions: (1) *Single*, where the digits appeared pseudo-randomly (equal transition probabilities between all digits. (2) In the *Triplet* condition the digits were presented in predefined chunks of three (4-5-6, 6-5-4, 7-8-9 and 9-8-7). (3) The *Nonet* condition then contained chunks of nine digits with each chunk consisting of three repeating Triplet chucks (4-5-6–4-5-6–4-5-6, 6-5-4–6-5-4–6-5-4, 7-8-9–7-8-9–7-8-9 and 9-8-7–9-8-7–9-8-7). (4) Finally, the *Complete* condition displayed the entire sequence of 36 digits in which all other conditions were nested in (4-5-6–4-5-6–4-5-6–-6-5-4–6-5-4–6-5-4–-9-8-7–9-8-7–9-8-7—7-8-9–7-8-9–7-8-9) (Fig. 2A). We generated de Bruijn sequences (Brimijoin and O'Neill, 2010; de Bruijn, 1946) to ideally pseudo-randomize (Aguirre et al., 2011) not only the transition between single digits and chunks but also the occurrence of the different blocks in the blocked presentation of the experimental conditions. In deviation to the passive watching paradigms usually applied in the context of TRW (e.g., Hasson et al., 2008), we included a task during the watching of the digit sequences. All sequences were pseudo-randomly interrupted by inserted zeros. The zeros acted as targets for the participants, who had to press a button upon seeing a zero, to keep their attention on the digits. The zero was chosen specifically due to its particular role among other numbers (Brysbaert, 1995; Nieder, 2016; Pinhas and Tzelgov, 2012). We included 18 targets per block of each experimental condition, so 360 zeros were presented during the entire fMRI experiment. The zeros were inserted in a way that we could control how often they interrupted a transition within and between chucks of the sequence.

The task consisted of 24 blocks, so that the subjects completed each experimental condition six times. Four blocks (each condition once) were presented outside the scanner as a training, while the remaining 20 blocks were then part of the main fMRI experiment in the scanner. We counterbalanced the first condition participants saw. Before each block subjects were presented with a fixation cross for a jittered duration of 6370–7950 ms. The fixation cross flashed three times to signal the start of the next block. The blocks themselves were then made up from sequences of 162 digits including the 18 targets. The sequences were presented in trials, one digit at a time. Each trial was 700 ms long. Digits

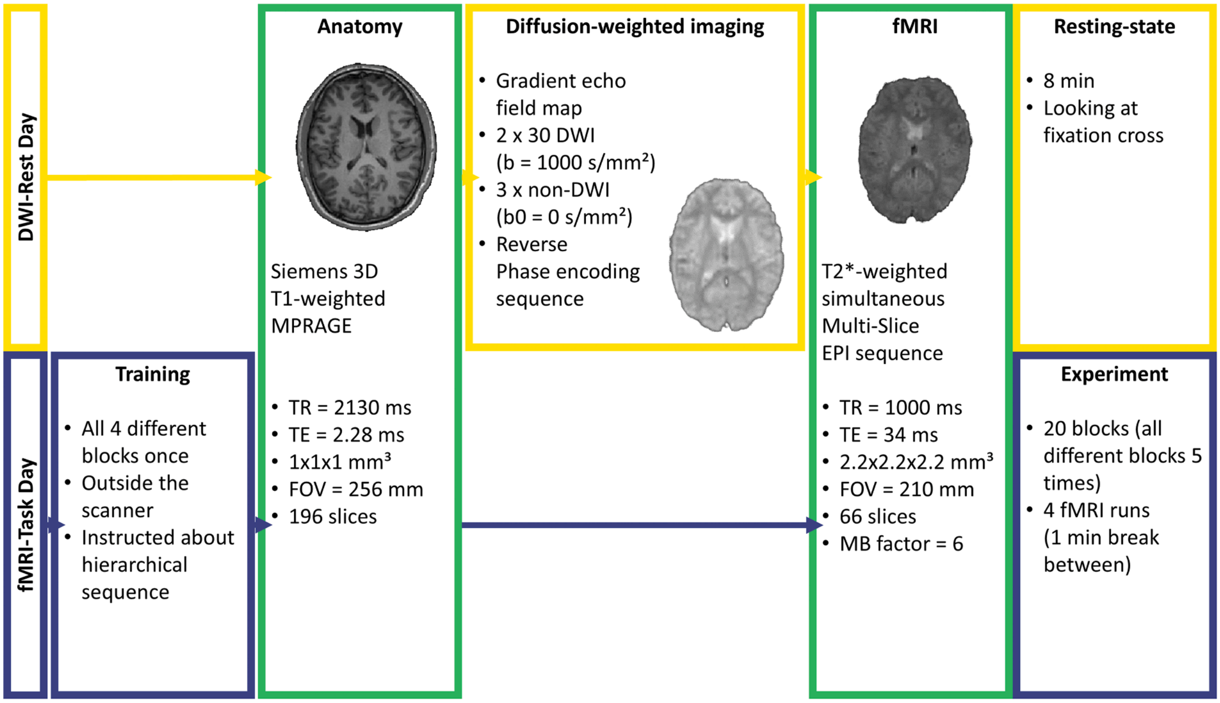

Fig. 1. Diagram of procedure during the scanning sessions DWI-Rest- and fMRI-Task-Day.
Note. MPRAGE = Magnetization prepared rapid acquisition gradient echo, TR = Time of repetition, TE = Echo time, FOV = Field of view, DWI = Diffusion-weighted imaging, EPI = Echo planar imaging, MB = Multiband. Note that the order of the two sessions was counterbalanced across participants.

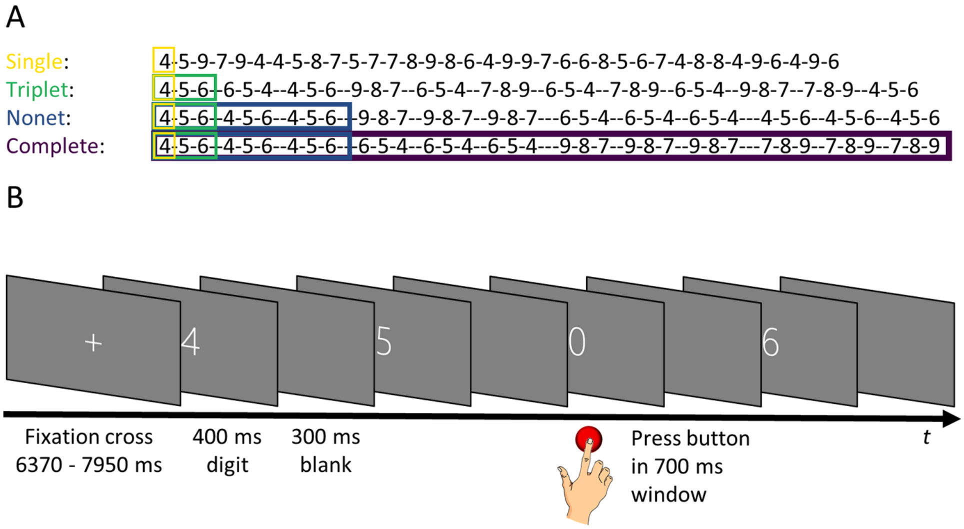

Fig. 2. Experimental paradigm on the fMRI-Task Day.
Note. (A) Example sequences for the four experimental conditions. Colors show nested hierarchical structure. (B) Presentation of digit sequence. Participants had to press a button when a 0 was presented.

were presented for 400 ms and followed by 300 ms of blank screen. The participants had the entire 700 ms to react if they saw a zero by pressing a button with their right index finger (Fig. 2B). As further motivation, the participants could win additional course credit or money on top of their standard renumeration based on their performance in the task. Lastly, we included a one-minute break after five blocks in the scanner in which the participants were informed about their progress in the experiment. In total, participants spent approximately 60 min in the scanner on the fMRI-Task-Day.

All digits and fixation crosses in both scanning sessions were displayed on a screen positioned behind the scanner bore and were viewed by the subjects through an adjustable 45° mirror at a visual angle of approximately 1.29°. Movements were minimized with form-fitting cushions. Subjects wore ear plugs and noise-cancelling headphones to reduce scanner noise.

2.1.3. *MRI data acquisition*

Brain images were recorded with a 3T Siemens Magnetom scanner (Siemens, Erlangen) using a 20-channel head coil. Functional blood-oxygen-level-dependent (BOLD) images during rs-fMRI and task-fMRI were acquired parallel to the anterior commissure/posterior commissure line. We used a T2*-weighted simultaneous multislice echo-planar imaging (SMS-EPI; 94 × 94 data acquisition matrix; 210 mm field of view (FOV); 57° flip angle; time of repetition (TR) = 1000 ms; echo time (TE) = 34 ms). Each volume consisted of 66 adjacent axial slices with a slice thickness of 2.2 mm, a gap of 0.11 mm (5 %), and a voxel size of 2.2 × 2.2 × 2.2 mm^3. Slice acquisition and multislice mode were interleaved. The acceleration factor was 6.

T1-weigthed anatomical images were acquired using a standard Siemens 3D MPRAGE sequence for a detailed reconstruction of anatomy with isotropic voxel size (1 × 1 × 1 mm) in a 256-mm FOV (256 × 256 matrix; 192 slices; 8° flip angle; TR = 2130 ms; TE = 2.28 ms).

For DWI, we applied the parameters of the imaging sequences used in the Marburg-Münster Affective Disorders Cohort Study (Vogelbacher et al., 2018). Imaging started with a gradient echo field map (320 mm FOV; 60° flip angle; TR = 616 ms; TE1 = 5.19 ms; TE2 = 7.65 ms; 56 slices, slice thickness = 2.5 mm; 0 mm gap; voxel size 2.5 × 2.5 × 2.5 mm^3; interleaved slice acquisition). This was followed by two times 30 DW images with a b-value of 1000 s/mm^2 and in total five non-DW images (b = 0 s/mm^2), that had the same parameters except for their b-value (320 mm FOV; initial rotation −90°; TR = 7300 ms; TE = 90 ms; 56 slices, slice thickness = 2.5 mm; 0 mm gap; voxel size = 2.5 × 2.5 × 2.5 mm^3; interleaved slice acquisition; GRAPPA acceleration factor = 2). DWI was completed by a Reverse Phase Encoding sequence (320 mm FOV; initial rotation −90°; TR = 7300 ms; TE = 90 ms; 56 slices, slice thickness = 2.5 mm; 0 mm gap; voxel size = 2.5 × 2.5 × 2.5 mm^3; interleaved slice acquisition; GRAPPA acceleration factor = 2).

2.1.4. *Cortical parcellation*

Parcellating the cortex allowed us to investigate and compare the cortical organizational schemes across different modalities in a common reference frame (Eickhoff et al., 2018; Glasser et al., 2016; Tzourio-Mazoyer et al., 2002). We applied recon-all from FreeSurfer (v7.2.0; Fischl, 2012) as well as functions from the Connectivity Analysis Toolbox (CATO, v3.1.2.; de Lange et al., 2023) on the individual T1-weigthed anatomical images to reconstruct and parcel the brain's surface. The quality of the individually parcellated cortical surfaces was controlled according to the ENIGMA protocols (https://enigma.ini.usc.edu/) by one of the authors (FM) and three student assistants. No data had to be excluded based on the quality control. CATO extends on the classical Desikan-Killiany parcellation (Desikan et al., 2006) that is included in FreeSurfer by the *Lausanne sub-parcellations* (Cammoun et al., 2012) which divide the larger parcel from the Desikan–Killiany atlas into equally sized smaller parcels for a higher resolution. For our analyses we specifically chose the *lausanne250* parcellation scheme as it showed exceptional reliability (Cammoun et al., 2012) and portrays a meaningful meso-level parcellation of the cortex (Amunts and Zilles, 2015). The application of the lausanne250 parcellation divided the brain into 219 cortical regions. Note that we did not include subcortical regions in the analysis as the DWI resolution would not have allowed for reliable estimation of streamlines (Kai et al., 2022).

2.2. *Resting-state fMRI and intrinsic timescales*

2.2.1. *Preprocessing*

For preprocessing the rs-fMRI data we made use of FSL (v6.0; Jenkinson et al., 2012) tools also within CATO (de Lange et al., 2023). For this we discarded the first five volumes as recommended for signal stabilization (Buxton, 2009; Caballero-Gaudes and Reynolds, 2017). The functional preprocessing in CATO included slice timing correction using FSL's sliceTimer and the application of FSL's MCFLIRT (Jenkinson et al., 2002) for the motion correction. The six estimated rigid motion correction parameters were used to calculate the framewise displacement and change in signal intensity between frames. The calculation of both motion metrics was based on Power et al. (2012). Additionally, an average of all motion corrected volumes was calculated and aligned with the individual T1-weigthed anatomical image. This alignment enables the registration of the functional data with the anatomical parcellation based on the structural data.

The slice time and motion corrected rs-fMRI data was then passed through a nuisance regression model (Ciric et al., 2017) to remove any unwanted influences on the data. To this end, we first extracted three masks from the individual anatomical images using the cortex parcellation from CATO: a whole brain, a white matter and a ventricle mask. For the regressors of nuisance we extracted the average time series from the white matter and the ventricles for each subject using these masks. Also, we calculated the first derivative of the six rigid motion correction parameters. Lastly, the rs-fMRI time series of each participant was de-meaned and de-trended. The nuisance regression model then removed the influence of the six rigid motion correction parameters and their six first derivatives as well as the quadratics of all variables. For noise reduction, a component-based method (CompCor; Behzadi et al., 2007) was applied on the extracted white matter and ventricle time series. The top five components of both the white matter and ventricle signals as well as their derivatives and quadratics were thus also removed as nuisance from the rs-fMRI data. Lastly, as recommended (Ciric et al., 2017), we included a spike regression according to Satterthwaite et al. (2013) in the model, removing every spike based on its framewise displacement.

Returning to CATO, we used the whole brain mask to extract the nuisance-corrected signal from cortical voxels. This signal was then bandpass filtered between 0.01 Hz and 0.1 Hz using a standard zero-phase Butterworth bandpass filter.

2.2.2. *Calculation of intrinsic timescales*

To analyze the distribution of intrinsic timescales across the cortex we first needed to extract the time series. Using CATO, we could obtain the individual, averaged time series from of the 219 cortical parcels from the lausanne250 parcellation (see Section 2.1.4). Based on these time series, we estimated the intrinsic timescale of each parcel via the decay of the autocorrelation function (ACF). We applied a model-free procedure (Raut et al., 2020) to determine the decay of the ACF. Applying the published code from Raut et al. (2020) we first de-meaned the nuisance-corrected rs-fMRI signal of every participant. We then determined the ACF by first calculating the lagged covariance in 24-s window for all lag $\Delta \epsilon [-12,12]$,

$$c_x(\Delta) = \frac{1}{T - |\Delta|} \sum_{t=1}^{T-|\Delta|} x(t+\Delta) * x(t) \tag{1}$$

before normalizing the results by the covariance at lag 0, so that $r_x(0) = 1$,

$$r_x(\Delta) = \frac{c_x(\Delta)}{c_x(0)} \tag{2}$$

The resulting $r_x(\Delta)$ can be interpreted as the lagged autocorrelation rather than covariance. The intrinsic timescale for each individual parcel was then determined as the precise abscissa of the ACF at $r_x(\Delta) = 0.5$, which describes the half of the full width at half maximum of the function. This calculation was achieved with the fnzeros function in MATLAB which computes the zeros of a spline fit of a function.

2.3. *Task-fMRI*

2.3.1. *Preprocessing*

Processing of the task data for the ISC analysis was based on the procedure described in Nastase et al. (2019). Preprocessing was completed using Statistical Parametric Mapping software (SPM12; FIL Methods Group, 2017) implemented in MATLAB (Version 9.10.0 [R2021a]; The MathWorks Inc., 2021) and included slice time correction to the spatially and temporally middle slice, realignment, co-registration to anatomical data, normalization to MNI space and smoothing using a $6 \times 6 \times 6$ mm^3 Gaussian smoothing kernel. The signal was further high-pass filtered at 1/160 s based on previous results (Mecklenbrauck et al., 2024). The nuisance regression in accordance with the recommendation (Nastase et al., 2019) included the six motion parameters estimated during realignment as well as the averaged white matter and cerebral-spinal-fluid signal. Additionally, we included all button presses of the subjects as a regressor of nuisance which was convolved with the canonical hemodynamic response function. For modelling, we applied the FAST algorithm to correct for autocorrelation as recommended for TR $\leq$ 1.4 s (Corbin et al., 2018). The following ISC analysis was performed on the residuals of the nuisance regression. In preparation of the ISC analysis, the residuals were z-scaled and masked with an average grey matter mask before concatenating the blocks of each experimental condition in the same order into a single four-dimensional file for each condition, synchronizing the digit presentation across subjects.

2.3.2. *Inter-subject correlation*

ISC is a measure of neural synchrony or reliability (Redcay and Moraczewski, 2020). The method requires a synchronized presentation of the same stimuli across subjects (Nastase et al., 2019). A high ISC value in a voxel then suggests that this voxel holds information about the presented stimulus as the synchronized stimulus is the only commonality between all participants which creates this correlation (Nastase et al., 2019). In the context of hierarchically structured stimuli, participants are presented with different hierarchically nested levels of the stimuli (e.g., Lerner et al., 2011). These levels differ by their temporal persistency, with hierarchically higher levels of the stimulus being more persistent (Uithol et al., 2012). Voxels that only depict higher ISC values in conditions that present more temporally persistent levels of the stimulus, have longer TRWs to process the longer persistence in the stimulus. Voxels with shorter TRWs on the other hand already have higher ISC values for more transient levels of the stimulus, but also show increased values for hierarchically higher levels, as the more transient levels are nested within the more persistent levels of the stimulus structure.

For the calculation of the ISC, we opted for the leave-one-out-method of ISC calculation to allow us later to apply classical statistical methods (Nastase et al., 2019; Thomas et al., 2018). Therefore, we adjusted available code (Nastase et al., 2019) to calculate individual ISC maps for each experimental condition. Finally, the ISC values were Fisher z-transformed to help with the normal distribution of the correlation values (Bond and Richardson, 2004). Based on these maps we extracted the average ISC value for each cortical parcel in the lausanne250 parcellation scheme. Therefore, we parcellated the individual normalized brains of each subject using the Multi-Scale Brain Parcellator (Tourbier et al., 2019), extracted the parcels as binary maps and dilated these maps three-dimensionally by one voxel size using functions from the WFU pick atlas toolbox (Maldjian et al., 2003) to accommodate for the smoothing of the data. These individual averaged ISC values for each parcel in each experimental condition were the basis of the following analyses.

2.4. *The six organizational schemes of interest*

As outlined in the introduction, our goal was to find a cortical organizational principle that best explains the distribution of intrinsic timescales and ISC values. We considered the following six candidate organizational schemes: (1) the RC architecture, (2) the DC architecture, (3) the uni-to-multimodal gradient, and (4) the posterior/lateral-to-anterior/medial gradient. Additionally, we explored the relationship of the chrontopy with (5) different graph theoretical measures of the individual structural networks as well as (6) cortical thickness as an approximation of cytoarchitectural differences (Wagstyl et al., 2015).

The extraction all organizational schemes will be described in the following sections.

2.4.1. Rich Club architecture

For the individual RC architecture (as well as the DC architecture (see Section 2.4.2) and graph theoretical measures of network centrality (see Section 2.4.5)), we first had to reconstruct the structural network from the estimated white matter streamlines.

2.4.1.1. Structural network reconstruction. To reconstruct the structural white matter network, we used the same pipeline as in Mecklenbrauck et al. (2024). Thus, we applied the structural pipeline from CATO (de Lange et al., 2023) which calls upon FreeSurfer (Fischl, 2012) and FSL (Jenkinson et al., 2012) for the structural (pre-)processing steps. Building on the reconstruction and parcellation of the cortical surface (see Section 2.1.4), the structural pipeline started by applying fslmerge, topup (Andersson et al., 2003; Smith et al., 2004) and eddy (Andersson and Sotiropoulos, 2016) of the FSL package to merge the DWI data and correct susceptibly as well as movement and eddy current artefacts. We then continued using CATO to reconstruct the white matter network using a combined diffusion tensor imaging (DTI) and generalized Q-sampling imaging (GQI; Yeh et al., 2010) model. This model showed the best benchmark results in respect to false positive and false negative streamlines (de Lange et al., 2023). GQI helps with solving the issue of multiple diffusion peaks in the case of crossing or kissing fibers. Thus, the combined method applied the classical informed RESTORE algorithm (Chang et al., 2005, 2012) for DTI modelling in cases of single diffusion peaks and opted for the GQI algorithm in more complex cases. The white matter tracts were then reconstructed deterministically using the FACT algorithm (Mori et al., 1999) adjusted for multiple diffusion peaks. The creation of connectivity matrices used the standard settings of CATO which are derived from van den Heuvel et al. (2013). Therefore, the algorithm started with eight seeds from each voxel included in the whole brain mask and followed the main diffusion direction to the next voxel until one of five stop cases occurred: (1) The algorithm reached a voxel with a low fractional anisotropy value ($FA < 0.1$), which often represents a grey matter voxel. (2) The reconstructed streamline exited the brain mask. (3) The streamline turned at an angle larger than 45°. (4) The reconstruction reentered a previously visited voxel. (5) The streamline reached the cerebellum. Only streamlines that fully connected two brain regions were considered for the connectivity matrices. The connectivity matrix of each subject was subsequently generated by combining these estimated streamlines with individual parcellated anatomical images. In accordance with the lausanne250 parcellation scheme we ended up with 219×219 connectivity matrices for each subject. Lastly, we controlled the individual structural connectivity matrices for outliers (van den Heuvel et al., 2019). No connectivity matrix showed any outliers, so all matrices were suitable for graph theoretical analysis.

2.4.1.2. Rich Club hub classification. The general procedure of the RC identification (Fig. 4A) was reported in Mecklenbrauck et al. (2024) and was inspired by Riedel et al. (2022). To summarize, we calculated the RC coefficient $\phi(k)$ in binarized structural connectivity matrices. The RC coefficient was then normalized based on the mean of 2500 random networks. The random networks were created by rewiring each connection of the empirical network ten times. Using the formula reported by van den Heuvel and Sporns (2011) we identified a range of degrees k, for which the empirical RC coefficient was significantly ($\alpha = 0.05$) larger than in the random networks. Significant evidence for this so-called RC regime (van den Heuvel and Sporns, 2011) indicated the presence of RC organization in the network. Based on this RC regime we used the previously described criteria (Mecklenbrauck et al., 2024; Riedel et al., 2022) to identify nodes of the network as possible hubs: (a) A node was in the top 15 % of highest degrees. (b) The degree of a node was at least as large as the start degree of the RC regime. (c) A node's degree was at least as large as the degree k with the largest normalized RC coefficient within the RC regime. (d) The node was within the top 33 % in four of five measures of node centrality: nodal degree/degree centrality, betweenness centrality, closeness centrality, between-module participation coefficient, and within-module degree z-score. The calculation of the participation coefficients and within-module degree z-degree requires the determination the module partition. Like Riedel et al. (2022), we identified this partition in a 60 % prevalence-based group-average network using the Louvain algorithm (Blondel et al., 2008). For this purpose, we first determined the optimal module resolution γ (Lurie et al., 2024). A higher resolution, so a larger value of γ, leads to a more nuanced module differentiation. We varied γ between the values of 0.5 and 3.5 (in increments of 0.1) using the Louvain algorithm (community_louvain.m) for module identification 1000 times per value of resolution γ. We then found the agreement between these 1000 partitions at each resolution γ (agreement.m). Using consensus-based clustering 100 times (consensus_und.m; $\tau = 0.6$), we identified a stable module partition at every level of resolution. To find the best resolution as describes by Lurie et al. (2024) we calculated the variation of information (Meilă, 2003), i.e., the similarity between the partition across all levels of resolution. The most representative module partition then was determined by the lowest median variation of information thus identifying the optimal module resolution γ. This most representative module partition was ultimately used for the calculation of the between-module participation coefficient and the within-module degree z-score. For the group-wise matrix in this case we determined the optimal $\gamma = 2.3$ (10 communities).

Importantly, the four hub definition criteria (a–d) introduced above do not necessarily result in a single consistent hub definition. To achieve this congruent definition, we applied additional criteria. Firstly, we only considered nodes that were labelled as hubs in at least three of the four criteria. Secondly and most vitally, we compared the proportions of edges between the identified hubs in the empirical structural with the inter-hub connections in the 2500 random networks. As the RC is defined by a particularly high connectivity between hub regions (Colizza et al., 2006), we used false discovery rate (FDR)-corrected Wilcoxon signed-rank test to test whether the possible hubs were more likely to connect to each other in the empirical network than in the 2500 random networks. The final set of *RC hubs* only contained nodes that were significantly more interconnected in the empirical network. We then classified nodes as *Feeder* nodes if they were directly connected to an RC hub but not part of the RC, and as *Local* nodes all nodes that were neither part of the RC nor connected to it.

In deviation to the previously applied identification (Mecklenbrauck et al., 2024), we classified the parcels as RC hub, Feeder node or Local node not in a group-averaged network but individual binarized connectivity matrices. Therefore, we binarized the individual matrices by setting every edge with at least three streamlines (Number of Streamlines ≥ 3) to one and all others to zero, as recommended for individual binarized connectivity matrices to correct for false positive edges (Brown et al., 2011). As described, following previous practice (Lurie et al., 2024; Riedel et al., 2022) only the module partition was based on the group-averaged binary connectivity matrix. This resulted in individual classifications of RC hubs, Feeder nodes and Local nodes. At this point, we had to exclude two participants from further analyses, as they did not depict RC architecture, reducing the sample size for the timescale analysis to $N_{RS} = 44$ and the ISC analysis to $N_{ISC} = 37$.

2.4.2. Diverse Club architecture

The procedure to identify DC hubs was in large parts similar to the RC hub identification (Fig. 5A). To determine if a DC architecture was present, we applied the modified clubness coefficient, that can calculate clubness not just on basis of the degree centrality but based on any nodal measure (Bertolero et al., 2017). Here we used the between-module participation coefficient as the nodal measure to identify a club of nodes which are particularly well connected with the modules of the network. As the module structure is central to the participation coefficient, we determined the optimal modularity not in a group-average network, like in the RC identification, but in each subject's network individually. As for the RC, we then normalized the DC coefficient on the basis of 2500 random networks using the same individual module classification for all random networks. We validated the presence of DC architecture in each subject by identifying a range of participation coefficients for which the empirical DC coefficient was significantly ($\alpha = 0.05$) larger than on average in the random networks; thus, mirroring the procedure for RC coefficients (van den Heuvel and Sporns, 2011). Furthermore, only one criterion was used to determine possible hubs: Following Bertolero et al. (2017) the top 20 % of the participation coefficient distribution was considered as a hub. Finally, to identify the DC hubs, we compared the proportions of inter-hub connections between the empirical and random networks, as we did for RC hubs. We only classified hubs as *DC hubs* if they connected to significantly more other hubs in the empirical network than in the random networks. Again, we used an FDR-corrected Wilcoxon signed-rank test to validate this comparison. Further, we also classified Feeder nodes and Local nodes based on the connections to the identified DC.

2.4.3. *Uni-to-multimodal gradient*

To identify parcels that are functionally classified as multimodal we used two different strategies: a data-driven approach using SFC (Fig. 6A1; Sepulcre et al., 2012) and an atlas-based approach employing the classification of functional modules introduced in Ji et al. (2019) (Fig. 6A2; Golesorkhi, Gomez-Pilar, Tumati, et al., 2021; Ito et al., 2020). Both approaches were validated by correlating the resulting uni-to-multimodal gradient maps with other previously established uni-to-multimodal gradients (Margulies et al., 2016; Sydnor et al., 2021; see Supplemental Material 1).

2.4.3.1. Stepwise functional connectivity. The SFC analysis calculates paths through the functional network starting at a seed region. It then maps the connectivity pattern of that seed region or multiple seed regions at different so-called link-step distances, so progressions of the connectivity along the calculated paths. In their seminal paper Sepulcre et al. (2012) demonstrated that when starting the paths in the primary visual, auditory and somatosensory cortices the paths reach a steady state after seven link-steps. The stable pattern of SFC converged in regions of the brain that can be described as cortical hubs or multimodal areas (e.g., Sepulcre et al., 2010). To capture the full spectrum of the uni-to-multimodal gradient from the SFC maps, we extracted the normalized SFC pattern at link-step one, which specifies the unimodal areas (Sepulcre et al., 2012), as well as the normalized SFC map at link-step seven to locate the multimodal hubs. Subtracting the SFC maps at the first step from the maps at link-step seven combines the topographies to portray the extent of the uni-to-multimodal gradient in one single map. The resulting values are higher for multimodal and lower for unimodal areas.

Therefore, we first aligned the individual, preprocessed and nuisance-regressed rs-fMRI data (see Section 2.2.1) to the MNI standard space using SPM12. In doing so, images were downsampled to a voxel resolution of $8 \times 8 \times 8$ mm^3. This downsampling rendered the voxel-wise connectivity matrices computationally manageable (Pretus et al., 2019; Sepulcre et al., 2012). We again used functions from CATO (de Lange et al., 2023) to extract the time course signal of 475 resting-state acquisition timepoints. The signal was extracted on the voxel level from a whole brain mask, which included 4575 $8 \times 8 \times 8$ mm^3 voxels. This signal was then filtered between 0.01 Hz and 0.1 Hz using a standard zero-phase Butterworth bandpass filter. For the SFC analysis we firstly calculated the individual 4575×4575 connectivity matrices using product-moment correlation. Only positive correlations were considered. Additionally, the correlations were Fisher z-transformed and then normalized between 0 and 1. To correct the adjacency matrix for false positive connections, we applied a conservative Bonferroni-correction at a significance level of $\alpha = 0.001$. Coherent with recent publications using SFC (Bueichekú et al., 2020; Diez and Sepulcre, 2018; Ortiz-Terán et al., 2017), we used these filtered weighted adjacency matrices for the analysis instead of binarizing them. We determined the normalized SFC at each link-step distance up to seven steps for each individual subject. As seed regions, we used the following MNI coordinates (x, y, z), identified based on the coordinated reported in Sepulcre et al. (2012) and further consultation of the SPM Anatomy Toolbox (Eickhoff et al., 2005): left visual (−8, −85, 4), right visual (8, −83, 4), left auditory (−47, −19, 8), right auditory (43, −32, 11), left somatosensory (−42, −29, 65) and right somatosensory (38, −29, 65). Each of these seeds was comprised of a single $8 \times 8 \times 8$ mm^3 voxel. To have a single SFC map per subject at each link-step we averaged the stepwise maps of all six seeds. We then subtracted the averaged, individual SFC maps at the first step from the maps at the seventh link-step to estimate the topography of the uni-to-multimodal gradient for each subject. Finally, we extracted the individual, averaged results from of uni-to-multimodal gradient maps for each parcel of the lausanne250 parcellation to arrive at a continuous representation of multimodality that can be related to the cortical chronotopy.

2.4.3.2. Ji atlas-based multimodality. The functional atlas introduced by Ji et al. (2019) is based on the Glasser atlas (Glasser et al., 2016). Each parcel in the surface-based Glasser atlas is assigned to one of twelve functional networks: Auditory, Visual1, Visual2, Somatomotor, Cingulo-Opercular, Default, Dorsal-Attention, Frontoparietal, Language, Orbito-Affective, Posterior-Multimodal, Ventral-Multimodal. In the distinction of unimodal and multimodal areas, previous papers labeled all parcels belonging to Auditory, Visual1, Visual2 and Somatomotor networks as unimodal or "periphery", and all others as multimodal or "core" (Golesorkhi et al., 2021a; Ito et al., 2020). To also assign the parcels of the lausanne250 parcellation to these categories, we determined the overlap between a parcellation of the MNI standard brain according to the Lausanne atlas (Cammoun et al., 2012) and a voxel-wise version of the Glasser atlas published by Horn (2016) and adjusted by Gorgolewski (2016). The comparison gave us a percentage for each parcel of the Lausanne atlas describing how much of its volume belonged to a multimodal area according to the definition by Ito et al. (2020). These percentages also described a continuous way of operationalizing multimodality to be related to the cortical timescales and ISC values.

2.4.4. *Posterior/lateral-to-anterior/medial gradient*

For the approximation of the posterior-to-anterior and lateral-to-medial gradients which are part of many theories on cortical organization (e.g., Alexander and Brown, 2018), we considered the average MNI coordinates of each parcel of a subject's cortex (Fig. 7A). Thus, we averaged the x-, y- and z- coordinates in FreeSurfer reference space (MNI305/fsaverage space; Fischl, 2012) of each parcel for each individual parcellation. We used the absolute values of the x-coordinate to model the lateral-to-medial trend, while an effect of the y-coordinate on the cortical chronotopy might signal a posterior-to-anterior trend, as was indicated previously (Mahjoory et al., 2020). The z-coordinates were used as control variables in all models.

2.4.5. *Graph theoretical measures of network centrality*

Furthermore, we considered graph theoretical measures of centrality of the parcels as explanatory variables. Therefore, we included the five nodal measures that were used in the identification of the RC (Mecklenbrauck et al., 2024; Riedel et al., 2022): degree centrality, betweenness centrality, closeness centrality, participation coefficient, and within-module degree z-score (Fig. 8A). For participation coefficient and within-module degree z-score we however used the individual optimal module distribution that was calculated for the DC identification.

2.4.6. Cortical thickness

The surface-based morphometry measures were calculated based on the surface tessellation using FreeSurfer (Dale et al., 1999). The cortical thickness can be calculated from the distance of the white matter surface and the pial surface, while the surface is described by the area of the vertices spanning the cortex (Fig. 9A; Goto et al., 2022). As a possible organizational scheme, we only explored the average cortical thickness (in mm) as it can be seen as an approximation for cytoarchitectural differences between the areas (Wagstyl et al., 2015) which were previously suggested to shape the cortical dynamics (Gao et al., 2020). The surface area (in mm^2) on the other hand was used as a control variable in all models of both the timescale and ISC analyses.

2.5. Statistical data analysis

2.5.1. Spin test analysis

To identify similarities between the six organizational schemes as well as the intrinsic timescales cortical and ISC values per experimental condition prior to the formal analysis we calculated Pearson correlation between all variables averaged over all subjects. As the RC and DC classifications are categorial variables we used the mode for each parcel instead of the mean. Also, we did not determine a correlation but used the Kruskal–Wallis-test and the χ^2-test of independence, respectively, to assess their relationship with the other continuous variables and between each other. Finally, we calculated the effect sizes of the test statistics (η^2 and Cramer's V; Tomczak and Tomczak, 2014) to compare them with the correlations. We tested the significance of these correlations and effect sizes via 100,000 spin test permutations (Alexander-Bloch et al., 2018) implemented in the neuromaps toolbox (Markello et al., 2022). The spin test accounts for the spatial autocorrelation of the cortical maps by rotating their spherical surface projection and thus creating a null distribution of the maps whilst keeping spatial features of the original map intact. The p-values of the test are then calculated by comparing how many of the permutated correlations, based on rotated maps, are equal or larger than the original correlation coefficient based on the initial orientation (Alexander-Bloch et al., 2018). Finally, we applied FDR correction (Benjamini and Hochberg, 1995) to correct the spin test results for multiple testing.

2.5.2. Resting-state timescale analysis

Data analyses were performed using R (Version 4.2.2.; R Core Team, 2022) and RStudio (Version 2022.7.2.576; RStudio Team, 2022). Bayesian hierarchical generalized linear modelling was executed using the brms library in R (Bürkner, 2017). All model equations were constructed from the same base formula:

$$\text{Resting-state timescales} \sim 1 + \textsc{Organizational Scheme} + \text{Surface area} + z\text{-Coordinate} + \text{ICV} + (1|\text{Subject}) \quad (3)$$

For the Organizational Scheme we were first interested in (1) the individual RC architecture of each subject. Second, the timescales were modelled by (2) the individual DC classification. The next set of models concerned in the effect of (3) the uni-to-multimodal gradient on the timescales. One model looked at the individually determined gradient calculated from SFC and the other uni-to-multimodal model included the percentage of each area that was part of a multimodal area according to the Ji atlas-based classification by (Golesorkhi et al., 2021a; Ito et al., 2020). Fourth, one model included the average x- and y-coordinates of each parcel, as well as their interaction to model (4) the posterior/lateral-to-anterior/medial gradient. Note that the absolute values of the x-coordinates were calculated to model a lateral-to-medial rather than a left-to-right gradient. Fifth, we built a model that included (5) all five centrality measures we considered. Finally, a model used (6) the areas' average cortical thickness as organization of interest. Additionally, all models controlled for the surface area and average z-coordinate of an area as well as the intracranial volume (ICV) of each participant and included a random intercept for each subject. All continuous independent variables were z-scaled for better interpretability of the intercepts.

We prepared the data by taking the natural logarithm of the timescales and excluded outliers (below $Q1 - 1.5 \times IQR$ or above $Q3 + 1.5 \times IQR$). The following inspection of the Cullen-Frey plots to judge the skewness and kurtosis of the data revealed that we could assume a distribution from the gaussian family for all models (Cullen and Frey, 1999). For estimating the models in brms we used uninformative priors as it is recommended for multilevel modelling (Bürkner, 2017). For β coefficients we used a flat prior and for the standard deviation a Student's $t(3, 0, 2.5)$ distribution was applied. All models were then calculated with ten chains, each with 4000 iterations, from which the first 1000 were warmups, setting the target average proposal acceptance probability (adapt_delta) to 0.99. Convergence within and between chains was examined through the improved convergence diagnostic $\widehat{R}$, with values under 1.05 indicating successful convergence (Vehtari et al., 2021). Further, we used posterior predictive checks to evaluate whether the models captured the observed data (Kruschke, 2011). We tested the effects of the different organizational schemes of interest on the intrinsic timescales using the hypothesis function from the brms library (Bürkner, 2017). Bayes factors for one-sided hypotheses are defined by the evidence ratio (Bürkner, 2018). Generally, evidence ratios >10 are considered strong evidence for the tested hypothesis (van Doorn et al., 2021).

(1) For the RC architecture, we expected that the areas classified as RC would show slower timescales than the areas classified as Feeder and Local nodes, while Feeder nodes also have slower timescales than in Local nodes (Gollo et al., 2015). (2) Likewise, for the DC architecture, we would envision the areas classified as DC to be the slowest, followed by Feeder nodes and then Local nodes. (3) Based on previous results (e.g., Ito et al., 2020), we assumed slower timescales with increasing multimodality for both uni-to-multimodal gradient approaches. (4) In the posterior/lateral-to-anterior/medial gradient model, we predicted the slowest timescales to be located to the medial frontal lobe (Mahjoory et al., 2020). So, we expected a positive trend for y-coordinates and negative trend for x-coordinates as well as negative interaction effect on the timescales. Based on prior findings related, a positive relationship between (5) the centrality measures (Fallon et al., 2020; Lurie et al., 2024) as well as (6) thicker cortical areas (Gao et al., 2020) and slower intrinsic cortical timescales could be suggested.

As it was the purpose of this study to find the best fitting organizational schemes, we did not specify a preferred model in advance, to not bias the analysis. However, judging from previous studies we expected the RC architecture to play a major role in shaping the intrinsic timescales of the cortex (e.g., Gollo et al., 2015).

2.5.3. Inter-subject correlation analysis

After inspection of the Cullen–Frey plots, we excluded outlier values (below $Q1 - 1.5 \times IQR$ or above $Q3 + 1.5 \times IQR$) to reduce kurtosis of the distribution (Cullen and Frey, 1999). In the same way as with the intrinsic timescales we modelled the distribution of ISC values by the different organization schemes of interest. Now we additionally included the Condition in interaction with the Organizational Scheme as an independent variable:

$$\text{ISC}_{\text{Fisher } z} \sim 1 + \textsc{Condition} \times \textsc{Organizational Scheme} + \text{Surface area} + z\text{-Coordinate} + \text{ICV} + (1|\text{Subject}) \quad (4)$$

The factor Condition included four levels: Single, Triplet, Nonet, and Complete. For the Organizational Scheme we focused on the same six organizational schemes of interest as for the resting-state timescales (see Section 2.5.2). The models further again included the surface area of each parcel in mm^2, the area's z-coordinates in MNI space, the intercranial volume of each participant in liters and a random intercept on the level of subjects as control. The continuous independent variables were again z-scaled.

The estimation of all models in brms used uninformative priors as it is recommended for multilevel modelling (Bürkner, 2017). For β coefficients we used a $N(0, 5)$ distributed priors while Student's $t(3, 0, 5)$ distribution was applied as prior for the standard deviations. We made use of the skewed normal family for the models. All models were then calculated with ten chains, each with 4000 iterations, with 1000 warmups. We left the target average proposal acceptance probability (adapt_delta) at the default of 0.8 but increased the maximal treedepth to 15. Convergence of the chains was monitored using the improved convergence diagnostic $\widehat{R}$ (Vehtari et al., 2021). Applying posterior predictive checks, we assessed the coherence between the modelled and observed data (Kruschke, 2011). We tested the effects of the different organizational schemes of interest on the ISC values across experimental conditions using the hypothesis function from the brms library (Bürkner, 2017).

Based on previous investigations on TRWs (Farbood et al., 2015; Hasson et al., 2015; Lerner et al., 2011), we generally expected that higher order structures in the organizational schemes are more involved in the processing of hierarchically higher structures in the stimuli, i.e., in the conditions Nonet and Complete. Specifically, we thus expected for the (1) RC and (2) DC classification that the ISC values in Local nodes do not differ across the experimental conditions, as the Local nodes handle the processing of more transient stimuli which are included in all hierarchically nested levels (Gollo et al., 2015). Further we assumed that the hubs in both classifications then show increased ISC values for hierarchically higher stimulus structures as hubs of the structural core are engaged by more persistent stimuli (Gollo et al., 2015). If the tested gradients better explained the processing of hierarchically structured stimuli we would expect (3) the uni-to-multimodal and (4) posterior/lateral-to-anterior/medial trends to be more pronounced for the processing of hierarchically higher stimuli structures, as the higher order regions only show an increase in ISC values with these more persistent stimuli (Wolff et al., 2022). In line with the timescale hypotheses, we would also expect that the effects of (5) the graph theoretical measures of centrality as well as (6) cortical thickness on the ISC values would be more pronounced for hierarchically higher conditions.

2.5.4. *Bayesian model comparison*

Finally, we compared the models using Bayesian statistics to find out which cortical organizational scheme best explains the respective distributions of resting-state timescales and ISC values across the cortex. Bayesian model comparison, in contrast to its frequentist counterpart, does not require the compared models to be nested and thus is ideal to evaluate different competing theories (Geweke, 2007; Hollenbach and Montgomery, 2020; Rouder et al., 2018). We ran leave-one-out-cross validations (LOO-CV) and used the results to estimate the *expected log pointwise predictive density* (elpd_{loo}) for each model. The elpd_{loo} describes a model's accuracy in predicting future, out-of-sample data and thus captures the goodness of fit of the model while also controlling for overfitting (Gelman et al., 2014). The elpd_{loo} value can be both positive or negative, with higher values (meaning closer to zero in the case of negative values) indicating a better predictive performance (Vehtari, 2024). To mitigate the high computational demands of cross-validations, LOO-CV can be approximated using Pareto smoothed importance sampling (Vehtari et al., 2017). When comparing models using elpd_{loo}, a model is considered better when the absolute difference in elpd_{loo} between the compared models is larger than one standard error ($se(\text{elpd}_{\text{loo}})$; Mohor et al., 2021).

3. Results

3.1. *Spin test*

The spin test results reporting the similarity between organizational schemes as well as the chronotopy are depicted in Fig. 3. A Kruskal–Wallis-test revealed that the intrinsic resting-state timescales differed significantly between the classifications as Local, Feeder or DC hub according to the DC architecture, $H(2) = 31.99$, $\eta_H{}^2 = 0.14$, $p_{\text{spin}} = 0.018$. Appropriately, also the participation coefficient correlated significantly with the resting-state-timescales, $r = 0.27$, $p_{\text{spin}} = 0.039$. Moreover, a χ^2-test showed that the DC classification and the RC classification in Local, Feeder and RC hub were significantly dependent, $\chi^2(2, N = 219) = 195.97$, $V = 0.67$, $p_{\text{spin}} = 0.003$. We also found that the SFC-based uni-to-multimodal gradient correlated significantly with the resting-state timescales, $r = 0.48$, $p_{\text{spin}} = 0.003$, and the Ji atlas-based estimation of the uni-to-multimodal gradient, $r = 0.52$, $p_{\text{spin}} = 0.002$. Additionally, the uni-to-multimodal-gradient based on SFC correlated negatively with the ISC values in the Single condition, $r = -0.31$, $p_{\text{spin}} = 0.027$, Triplet condition, $r = -0.31$, $p_{\text{spin}} = 0.006$, Nonet condition, $r = -0.31$, $p_{\text{spin}} = 0.012$, and Complete condition, $r = -0.43$, $p_{\text{spin}} = 0.003$. Furthermore, the spin test revealed that the percentage of overlap with a multimodal area in the Ji atlas (Ji et al., 2019) correlated significantly negatively with the ISC values in the Complete conditions, $r = -0.43$, $p_{\text{spin}} = 0.006$.

Beyond that, we found several significant correlations between the graph theoretical measures of centrality. The degree centrality correlated significantly with closeness centrality, $r = 0.72$, $p_{\text{spin}} = 0.001$, betweenness centrality, $r = 0.79$, $p_{\text{spin}} = 0.001$, participation coefficient, $r = 0.59$, $p_{\text{spin}} = 0.002$, and within-module degree z-score, $r = 0.79$, $p_{\text{spin}} = 0.001$. Closeness centrality correlated also with betweenness centrality, $r = 0.79$, $p_{\text{spin}} = 0.001$, the participation coefficient, $r = 0.76$, $p_{\text{spin}} = 0.002$, and the within-module degree z-score, $r = 0.33$, $p_{\text{spin}} = 0.001$. Lastly, the correlations of betweenness centrality with the participation coefficient, $r = 0.76$, $p_{\text{spin}} = 0.002$, and the within-module degree z-score, $r = 0.46$, $p_{\text{spin}} = 0.001$, were also significant.

Finally, all the ISC values of the different experimental conditions were significantly correlated with each other. The ISC values of the Single condition shared correlations with the Triplet, $r = 0.76$, $p_{\text{spin}} = 0.002$, Nonet, $r = 0.83$, $p_{\text{spin}} = 0.002$, and Complete conditions, $r = 0.79$, $p_{\text{spin}} = 0.002$. The values of the Triplet condition correlated with the values in the Nonet, $r = 0.82$, $p_{\text{spin}} = 0.002$, and Complete conditions, $r = 0.81$, $p_{\text{spin}} = 0.003$. Also, the ISC values of the Nonet and Complete conditions were significantly correlated, $r = 0.84$, $p_{\text{spin}} = 0.002$. Note, reported p-values of the spin tests are FDR-corrected.

3.2. *Results of the six organizational schemes*

All models successfully converged as evaluated by the convergence diagnostic $\widehat{R}$ (Vehtari et al., 2021; for more details see Supplemental Tables S2.1 & S2.2). Graphical assessment affirmed that the predictive posterior distributions reasonably replicated the distributions as well as the means of the observed data (Supplemental Figs. S3.1–S4.8). Examining the multicollinearity resulted in no variance inflation factors over the threshold of ten (Wooldridge, 2013; Supplemental Figs. S3.1–S3.8). To test our hypotheses about the different organizational schemes we drew posteriors from the estimated models (Supplemental Tables S2.1 & S2.2).

3.2.1. *Rich Club architecture*

Beginning with the resting-state timescales, for the RC architecture the hypothesis tests revealed a significance increase in timescales between Local nodes and Feeder nodes as well as a significantly slower timescales in RC hubs than Local nodes, while RC hubs did not differ from Feeder nodes (Fig. 4B).

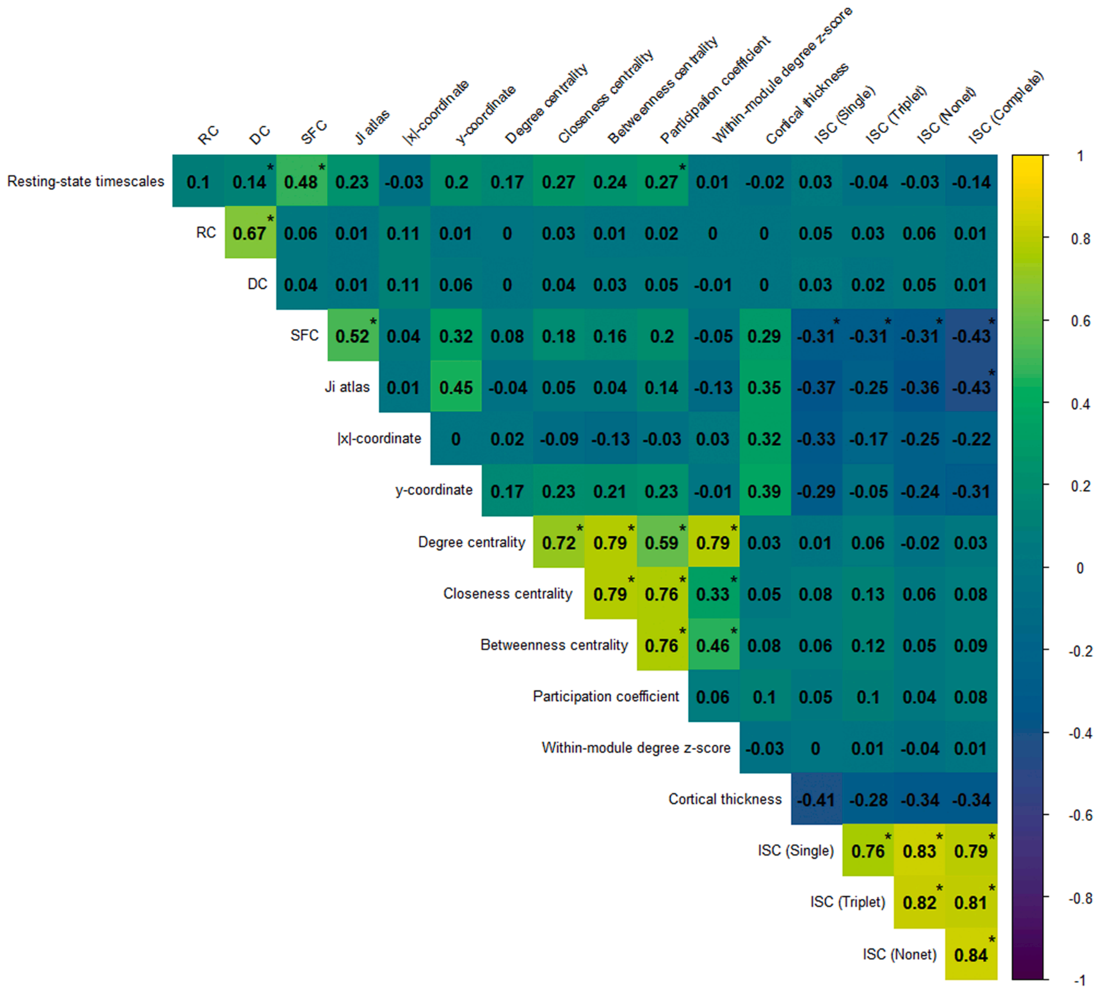

	RC	DC	SFC	Ji atlas	|x|-coordinate	y-coordinate	Degree centrality	Closeness centrality	Betweenness centrality	Participation coefficient	Within-module degree z-score	Cortical thickness	ISC (Single)	ISC (Triplet)	ISC (Nonet)	ISC (Complete)
Resting-state timescales	0.1	0.14*	0.48*	0.23	-0.03	0.2	0.17	0.27	0.24	0.27*	0.01	-0.02	0.03	-0.04	-0.03	-0.14
RC		0.67*	0.06	0.01	0.11	0.01	0	0.03	0.01	0.02	0	0	0.05	0.03	0.06	0.01
DC			0.04	0.01	0.11	0.06	0	0.04	0.03	0.05	-0.01	0	0.03	0.02	0.05	0.01
SFC				0.52*	0.04	0.32	0.08	0.18	0.16	0.2	-0.05	0.29	-0.31*	-0.31*	-0.31*	-0.43*
Ji atlas					0.01	0.45	-0.04	0.05	0.04	0.14	-0.13	0.35	-0.37	-0.25	-0.36	-0.43*
|x|-coordinate						0	0.02	-0.09	-0.13	-0.03	0.03	0.32	-0.33	-0.17	-0.25	-0.22
y-coordinate							0.17	0.23	0.21	0.23	-0.01	0.39	-0.29	-0.05	-0.24	-0.31
Degree centrality								0.72*	0.79*	0.59*	0.79*	0.03	0.01	0.06	-0.02	0.03
Closeness centrality									0.79*	0.76*	0.33*	0.05	0.08	0.13	0.06	0.08
Betweenness centrality										0.76*	0.46*	0.08	0.06	0.12	0.05	0.09
Participation coefficient											0.06	0.1	0.05	0.1	0.04	0.08
Within-module degree z-score												-0.03	0	0.01	-0.04	0.01
Cortical thickness													-0.41	-0.28	-0.34	-0.34
ISC (Single)														0.76*	0.83*	0.79*
ISC (Triplet)															0.82*	0.81*
ISC (Nonet)																0.84*

Fig. 3. Results of the exploratory spin tests.
Note. For Rich Club and Diverse Club effect sizes (η^2 and Cramer's V) are reported instead of Pearson correlation coefficient. RC = Rich Club, DC = Diverse Club, SFC = Stepwise functional connectivity, ISC = Inter-subject correlation, * $p_{\text{FDR}} < 0.05$.

Looking at the results for the ISC values, the tests revealed no significant differences between RC hubs, Feeder nodes and Local nodes in any experimental condition. Only testing for equal ISC values between conditions showed significant results, which suggests that we could not find an increase of ISC values of the temporal persistency of hierarchically structured stimulus in neither RC hubs nor Feeder nodes (Fig. 4C).

3.2.2. Diverse Club architecture

Regarding the resting-state timescales, we found a significant increase in the estimated mean timescale between Local nodes and DC hubs and between Feeder nodes and DC hub, while Local nodes did not differ from Feeder nodes (Fig. 5B).

The task data revealed a very similar pattern to the RC architecture. The Local nodes, Feeder nodes and DC hubs did not differ in their ISC values. Also, no significant increase of ISC values was found between the experimental conditions for any of the node classification (Fig. 5C).

3.2.3. Uni-to-multimodal gradient

For the resting-state timescales both approaches at modelling this gradient revealed a significant increase of intrinsic timescales with a higher value of multimodality (Fig. 6B).

Also, in the analysis of ISC values the two approaches at modelling multimodality produced largely similar results. The hypothesis test for both models revealed significantly negative effects of multimodality on the ISC values, in the Single, Triplet and Complete conditions, while the effect in the Nonet condition was only significantly negative for the model using the Ji atlas (Ji et al., 2019). So, an increase in multimodality predicted a decrease in the ISC value. When comparing the effects between the conditions, both approaches identified an increase in the influence of multimodality on the ISC value between the Single and Triplet conditions. Additionally, only for the SFC model the test also showed a significantly larger effect of multimodality in the Nonet compared to the Triplet condition (Fig. 6C).

3.2.4. Posterior/lateral-to-anterior/medial gradient

The resting-state timescales model for the posterior/lateral-to-anterior/medial gradient did not reveal an effect of the absolute x-coordinate but displayed significantly longer timescales with an increase in the y-coordinate as well as significant negative interaction between the absolute x-coordinate and the y-coordinate (Fig. 7B).

Looking at the task data, the results depicted a significantly negative effect of the absolute x-coordinate in all experimental conditions but the Triplet condition. Also, the effect of the y-coordinate was significantly negative in all conditions except for Triplet while the interaction effect on the ISC values was only significantly negative in the Single and Complete conditions. When comparing the effects between the experimental conditions, we found a significant decrease of the effect of the absolute x-coordinate on the ISC value between the Triplet and Nonet conditions. Also, the interaction effect decreased significantly between these two experimental conditions. The effect of the y-coordinate however increased between the Single and Triplet conditions (Fig. 7C).

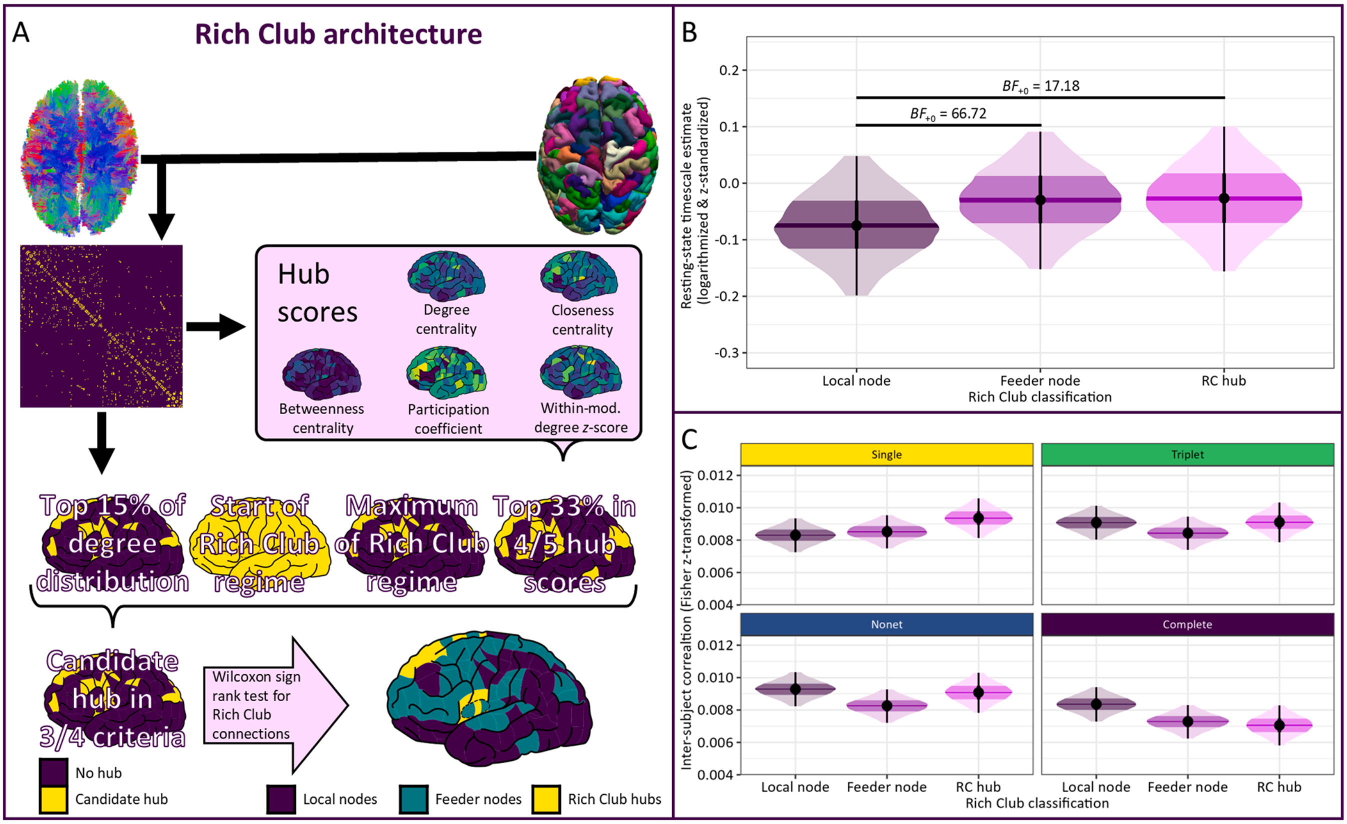

Fig. 4. Methods for extraction and results of intrinsic resting-state timescale and inter-subject correlation analyses for Rich Club architecture.
Note. (A) Rich Club (RC) identification was performed on individual binarized structural connectivity matrices with 219 cortical nodes according to the lausanne250 parcellation scheme (Cammoun et al., 2012). A combination of four different nodal cutoffs (top 15 % of degree distribution, start of RC regime, maximum of RC regime, top 33 % in at least four of five hubscores/nodal measures of centrality) resulted in a set of candidate hub. The final RC hubs were determined by testing if hub connections were more likely than expected at random in compliance with the RC definition (Colizza et al., 2006). (B) Density plots of the posterior distributions of node classifications according to Rich Club architecture with mean point estimate, 50 % and 95 % highest probability density areas marked. (C) Plots are arranged according to CONDITION. Density plots of the posterior distributions of node classifications according to Rich Club architecture with mean point estimate, 50 % and 95 % highest probability density areas marked. RC = Rich Club, BF = Bayes factor.

3.2.5. Graph theoretical measures of network centrality

In the resting-state model including all considered graph theoretical measures of centrality we detected a significantly positive effect of betweenness centrality as well as closeness centrality on the length of the timescales (Fig. 8B).

For the task-data, none of the effects of any graph measure in any experimental condition differed from zero. Comparing the conditions on the other hand revealed a significant increase of the effect of degree centrality on the ISC value between the Single and Triplet as well as an increase of the effect of the participation coefficient between the Nonet and Complete conditions (Fig. 8C).

3.2.6. Cortical thickness

Finally, modelling the effect of cortical thickness on the resting-state timescales revealed a significant increase of intrinsic cortical timescales with the average cortical thickness of an area (Fig. 9B).

Analyzing the ISC values, the two-sided hypothesis tests for the model using cortical thickness as the explanatory variable unveiled significant decreases of ISC values with the area's average cortical thickness in all conditions. In the comparison of the experimental conditions however we could not identify any increase in the influence of the cortical thickness on the ISC values between any of the tested conditions (Fig. 9C).

3.3. Model comparison

Additionally to the hypothesis tests, we compared the estimated models to find the organizational schemes that best explain the distribution of intrinsic timescales as well as ISC values across the cortex.

3.3.1. Resting-state timescales

Comparing the elpd_{loo} (Vehtari et al., 2017) of the intrinsic cortical timescale models identified that modelling the uni-to-multimodal gradient using the overlap of each parcel with a multimodal area according to the Ji atlas (Ji et al., 2019) as an estimation of multimodality as the best fitting model (Table 1). Inspecting the differences in elpd_{loo} showed that this model performed significantly better than the null model only containing the control variables as well as the models for the RC and DC architectures, as the difference was larger than one standard error (Mohor et al., 2021). All other models however did not perform significantly worse than the Ji atlas model (Fig. 10A).

3.3.2. Inter-subject correlation values from task-fMRI data

We also examined the elpd_{loo} to compare the models of the ISC values across the four experimental conditions. The results revealed that modelling the uni-to-multimodal gradient using the Ji atlas (Ji et al., 2019) approach most accurately predicted the distribution of ISC values (Table 2). The elpd_{loo} of this model was significantly larger compared with all other models. The second-best model was the posterior/lateral-to-anterior/medial gradient modelled via the MNI space coordinates which still fitted the data significantly better than the other organizational schemes. The model using the cortical thickness as an approximation for cytoarchitectural differences came in third and fitted the ISC values also significantly better than the models

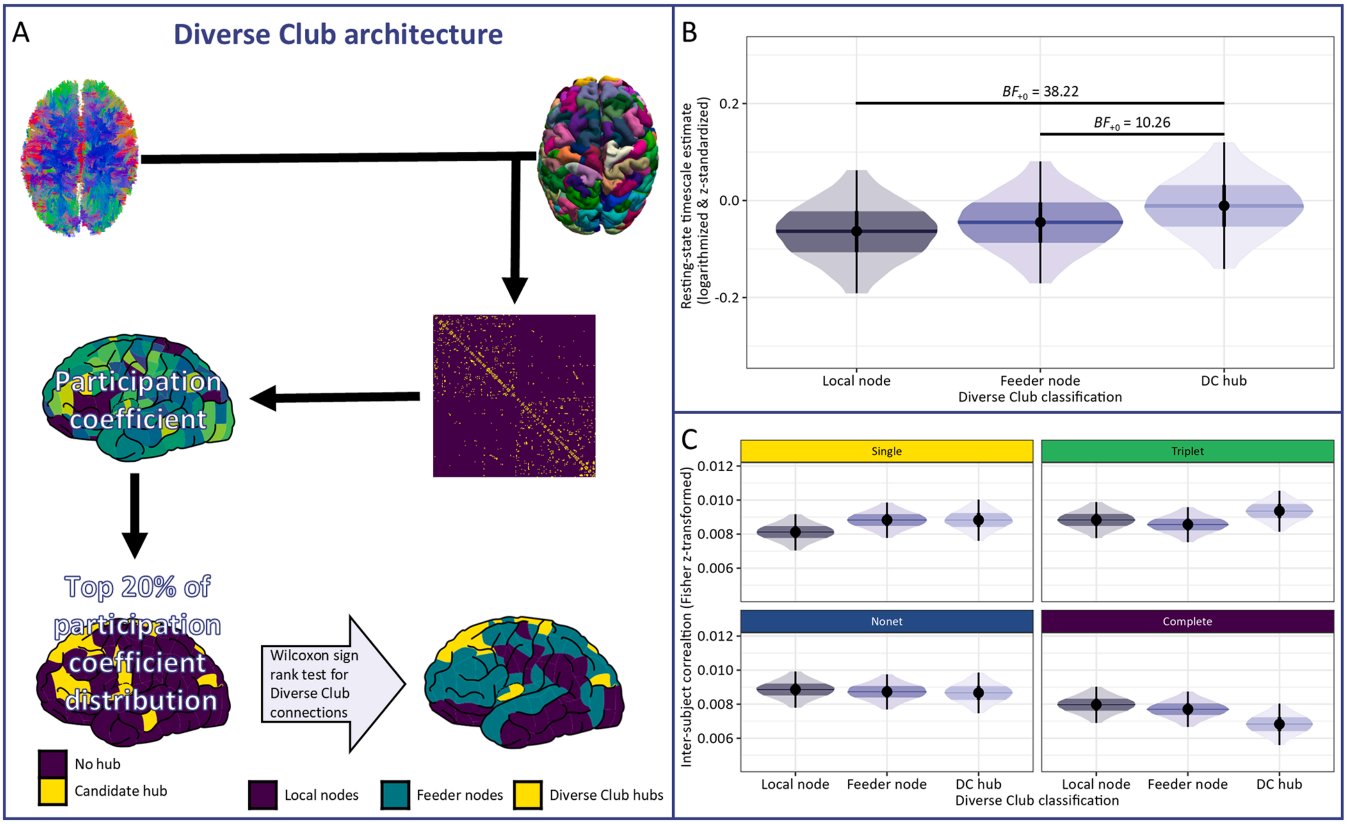

Fig. 5. Methods for extraction and results of intrinsic resting-state timescale and inter-subject correlation analyses for Diverse Club architecture.
Note. (A) Diverse Club (DC) identification was performed on individual binarized structural connectivity matrices with 219 cortical nodes according to the lausanne250 parcellation scheme (Cammoun et al., 2012). Using the top 20 % of the participation coefficient distribution resulted in a set of candidate hubs. The final DC hubs were determined by testing if hub connections were more likely than expected at random like in the Rich Club identification. (B) Density plots of the posterior distributions of node classifications according to Diverse Club architecture with mean point estimate, 50 % and 95 % highest probability density areas marked. (C) Plots are arranged according to Condition. Density plots of the posterior distributions of node classifications according to Diverse Club architecture with mean point estimate, 50 % and 95 % highest probability density areas marked. DC = Diverse Club, BF = Bayes factor.

representing the RC and DC architectures, the model including the graph theoretical measures of centrality as well as the null model. All other models did not significantly differ from the null model that contained no explanatory organizational scheme (Fig. 10B).

4. Discussion

Intrinsic timescales of the human brain may underly our capacity to process the complex temporal structure of our environment (Golesorkhi et al., 2021b; Wolff et al., 2022), but we do not know how they actually arise. In this paper we examined six different cortical organizational schemes and features of the cortical areas to investigate their role in shaping the cortical timescales at rest as well as during a task presenting stimuli of varying temporal persistence. The following discussion will highlight the key findings while also discussing the individual organization schemes more in depth.

4.1. The uni-to-multimodal gradient best explains the cortical chronotopy

The aim of this paper was to find the organizational scheme that best explains the chronotopy of the cortex. The Bayesian model comparison of all considered organizational schemes identified the uni-to-multimodal gradient modelled by the Ji atlas-based classification to be the best fitting model for both the resting-state timescales and the distribution of ISC values in the task-based fMRI data. This corroborates previous results finding the uni-to-multimodal gradient for the distribution of timescales (Gao et al., 2020; Golesorkhi et al., 2021a; Ito et al., 2020; Raut et al., 2020) as well as for TRWs (Farbood et al., 2015; Hasson et al., 2004, 2008; Lerner et al., 2011). A gradient from the primary sensory cortices to multimodal association cortices is a well-established concept in neuroscience (Huntenburg et al., 2018; Margulies et al., 2016; Mesulam, 1998; Sepulcre et al., 2012). Traversing from unimodal over supramodal to multimodal cortices (Zamora-López et al., 2011), the gradient's apex is assumed to be located within the limbic system (Chanes and Feldman Barrett, 2016; Margulies et al., 2016; Mesulam, 1998). In functional terms, the multimodal cortices are considered particularly important for the integration of information and for the retention and retrieval of past information (Murphy et al., 2019; Wang, 2020). Moreover, the activity of areas higher on the gradient is less stimulus-determined and relates more to abstract and domain-general processes (Taylor et al., 2015; Yeo et al., 2015), while it was proposed that these areas perform similar tasks among various domains (Goldman-Rakic, 1988). Besides the cortical timescales (e.g., Raut et al., 2020), many other, especially microarchitectural features like cortical thickness, neuron density (Burt et al., 2018; Wagstyl et al., 2015) and myelinization (Demirtaş et al., 2019; Huntenburg et al., 2017; Ito et al., 2020) as well as gene expression gradients (Burt et al., 2018; Hansen et al., 2021; Shafiei et al., 2020) were found to follow an uni-to-multimodal axis (for more information see Huntenburg et al., 2018; Markello et al., 2022; Sydnor et al., 2021).

Despite the consistency and comprehensiveness of previous findings, the question remains how exactly timescales are shaped along this gradient. Previous modelling work was able to establish, that timescales are driven by both local excitatory connections as well as by long-range connections of an area (Chaudhuri et al., 2015; Schmidt et al., 2016; for reviews see Cavanagh et al., 2020; Duarte et al., 2017). On the local

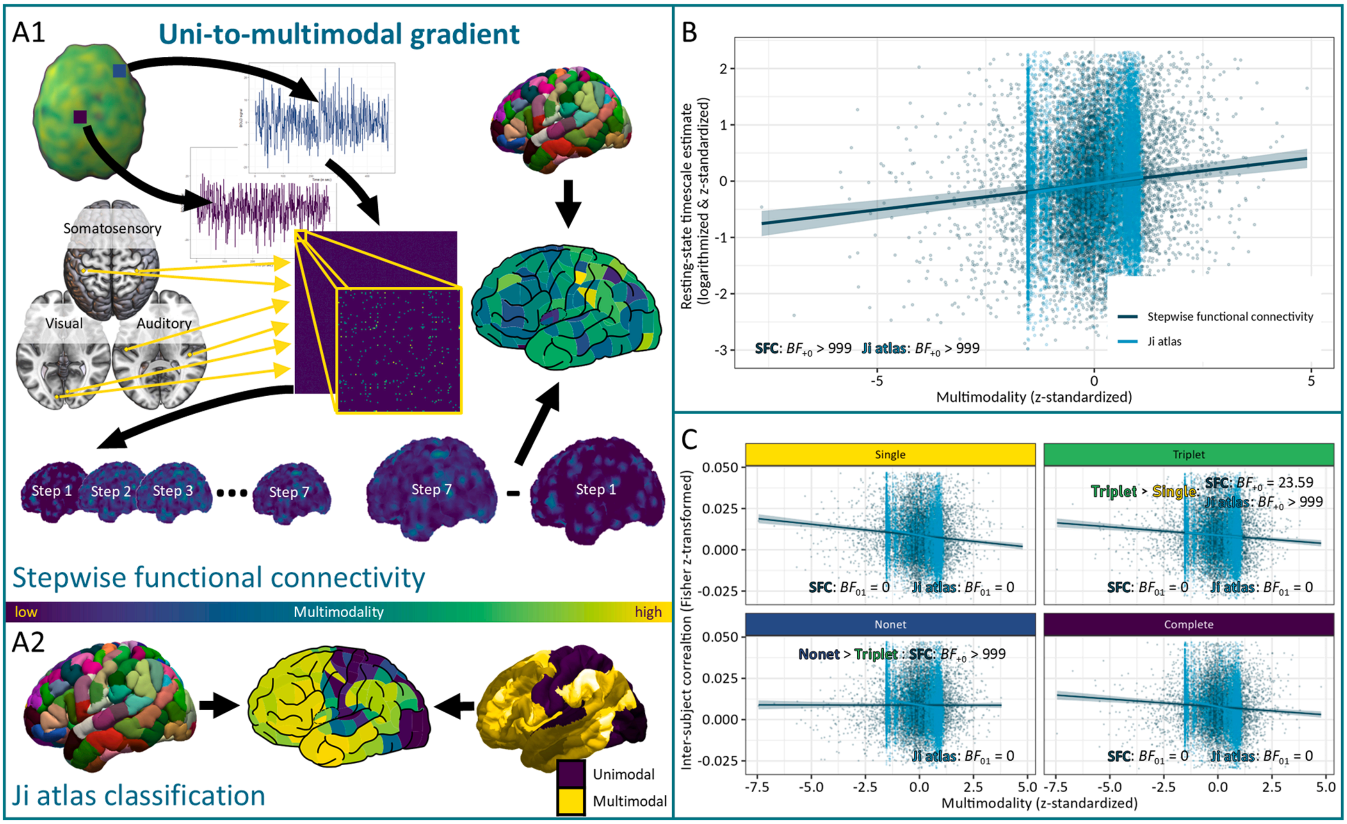

Fig. 6. Methods for extraction and results of intrinsic resting-state timescale and inter-subject correlation analyses for uni-to-multimodal gradient.
Note. Two approaches at modelling the uni-to-multimodal gradient as a constant measure of multimodality: (A1) First, stepwise functional connectivity follows network path through individual voxel-wise functional connectivity networks starting in seeds in the primary auditory, somatosensory and visual cortices. Paths converge in multimodal areas after seven link-steps. Individual uni-to-multimodal gradients were estimated by subtracting the stepwise functional connectivity values at first link-step from the values at the seventh link-step. Results were extracted using the lausanne250 parcellation scheme to model multimodality. (A2) Second, we considered the Ji atlas (Ji et al., 2019) based classification assorting cortex into uni- and multimodal areas. The overlap of classification in the Ji atlas and lausanne250 parcellation scheme was used as the second approach at modelling multimodality. (B) Fixed effect predictions of stepwise functional connectivity and Ji atlas approaches to model uni-to-multimodal gradient with 95 % credibility interval marked. (C) Plots are arranged according to Condition. Fixed effect predictions of stepwise functional connectivity and Ji atlas approaches to model uni-to-multimodal gradient with 95 % credibility interval marked. SFC = Stepwise functional connectivity, BF = Bayes factor.

scale, the ratio of excitatory pyramidal interneurons was found to increase with the cortical hierarchy (Torres-Gomez et al., 2020). These interconnected excitatory pyramidal cells in granular level III were also proposed to possess different ratios of neuronal receptors across the cortex (Cavanagh et al., 2020; Wang, 2001). Thereby, especially the density of glutaminergic NMDA receptors plays a crucial role for slower and maintained cortical dynamics of these pyramidal cells (Wang, 2001). Interestingly, the distribution of NMDA receptors was suggested to increase along the uni-to-multimodal gradient as well (Burt et al., 2018; Wang et al., 2012). Based on these findings, Wang (2020) concisely illustrated that the association cortices have more excitatory inter-neuronal connections as well as more input controlling inhibitory connections, while sensory cortices have more output-controlling connections. Similar to Gollo et al.'s (2015) proposal for RC architecture, this connectivity pattern enables the association cortices to produce slower intrinsic timescales while also having the ability of integrate information over longer periods of time. As these results clearly indicate the importance of the dynamics on the neuronal level, investigating the timescales on the microscale promises fruitful results to aid in the deeper understanding of the biological and connective mechanisms behind the temporal hierarchy of the cortex.

While we identified the Ji atlas approach as the best fitting model, we also examined the SFC approach to the uni-to-multimodal gradient. Using SFC, previous studies could show that paths starting from unimodal seed regions converge in multimodal areas after seven steps (Diez and Sepulcre, 2018; Pretus et al., 2019; Sepulcre, 2014; Sepulcre et al., 2012). To determine a gradient from the unimodal seeds to the multimodal cortices, we subtracted the initial SFC pattern at link-step one, which determines the unimodal areas, from the pattern at link-steps seven, which localizes the multimodal cortices. In contrast, the Ji atlas describes the classification of twelve functional networks based on neurobiological data, defining multimodality by these networks (Ji et al., 2019). Despite these considerable differences in approaching the concept of the uni-to-multimodal gradient, we were able to confirm the validity of both these methods by comparing the resulting uni-to-multimodal gradients with previously discovered gradients (see Supplemental Material 1; Margulies et al., 2016; Sydnor et al., 2021). Moreover, we also find largely coherent results between the two approaches. Both models predicted an increase of the intrinsic resting-state timescales with a higher multimodality and generally showed a decrease of ISC values with an increase in multimodality across the experimental conditions. Also, when exploring the relationship between the organizational schemes using the spin test approach (Alexander-Bloch et al., 2018) we found a significant correlation between the group average patterns of the two multimodality approaches. Therefore, the question remains as to why the SFC model did not perform as well as the Ji atlas approach in the model comparison. Based on the presented results, we speculate that there are still some methodological differences between the two approaches that could explain remaining divergences between the gradients. Firstly, for the SFC approach we determined

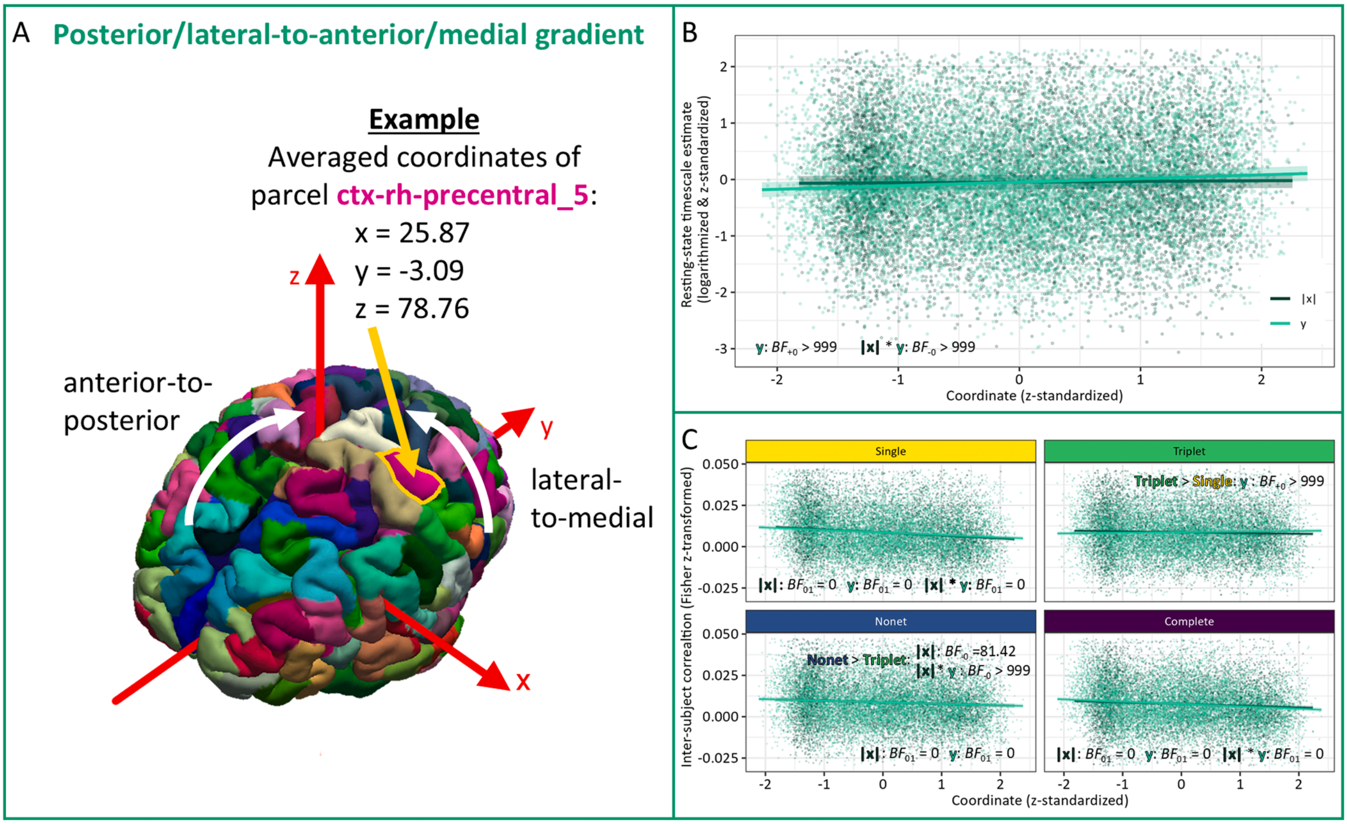

Fig. 7. Methods for extraction and results of intrinsic resting-state timescale and inter-subject correlation analyses for posterior/lateral-to-anterior/medial gradient. *Note.* (A) The lateral-to-medial and posterior-to-anterior gradients were modelled by using the averaged, individual *x*- and *y*-coordinates of each parcel, respectively. Absolute *x*-coordinates were used to model a lateral-to-medial rather than a left-to-right trend. (B) Fixed effect predictions of $|x|$- and *y*-coordinates to model lateral-to-medial and posterior-to-anterior gradients with 95 % credibility interval marked. (C) Plots are arranged according to CONDITION. Fixed effect predictions of $|x|$- and *y*-coordinates to model lateral-to-medial and posterior-to-anterior gradients with 95 % credibility interval marked. BF = Bayes factor.

multimodality values for each individual subject while the Ji atlas-based multimodality scores were the same for the entire group. The group-wise approach might have the advantage that global patterns of cortical organization are better revealed in group average networks (Hagmann et al., 2008). Secondly, the different spatial resolution of the two modelling approaches can be critical. The SFC approach requires the creation of downsampled voxel-wise connectivity matrices, which is a significant but computationally necessary limitation (Pretus et al., 2019). The Ji atlas on the other hand was originally based on state-of-the art parcellation of the data (Glasser et al., 2016). Thirdly, the definition of multimodality differs between the two approaches: Multimodal areas in the SFC approach describe the final step in the functional hierarchy (Sepulcre et al., 2012), while the Ji atlas-based classification defines all but the purely sensory networks as multimodal (Golesorkhi et al., 2021a; Ito et al., 2020). As the deployed task may not have been able to engage the apex of the processing hierarchy (as discussed in more detail in Section 4.3), the broader classification of multimodality in the Ji atlas-based gradient might have been more fitting especially to the distribution of ISC values.

On a different note, we only investigated two of many possible ways to define the uni-to-multimodal gradient. In validating the two here applied approaches we performed an additional analysis comparing the group-average uni-to-multimodal maps from the described analysis with two previously established gradients (see Supplemental Material S1). For this we used the gradients from Margulies et al. (2016), that are based on the decomposition of functional connectivity data into principal gradients, and Sydnor et al. (2021), who integrated multiple measures defining the gradient into one converging uni-to-multimodal map. We found that both our approaches to the uni-to-multimodal gradient significantly correlated with these two established gradients, that were previously also related to the chronotopy of the cortex (Fehring et al., 2024; Huntenburg et al., 2018). Therefore, the results not only validate the chosen approaches but further highlight the importance of the uni-to-multimodal gradient as a cortical organizational scheme. Beyond these four different approaches there is still a multitude of other functional and structural features can be used to define the uni-to-multimodal gradient (Sydnor et al., 2021). Thus, also the selection of six organizational schemes we investigated in this study only makes up a fraction of possible organizations. Moreover, we used Bayesian model comparison to find the best organizational scheme. While Bayesian model comparison in general allows for the comparison of non-nested models and thus is perfectly suited for comparing different theories or competing organizational schemes like in this paper (Geweke, 2007; Hollenbach and Montgomery, 2020; Rouder et al., 2018), model comparison is not able to detect the "true" model for the data. It is bound to the model space and will only identify the best fitting among the evaluated models (Alston et al., 2004). There could be a plethora of other organizational patterns and structures that could explain cortical timescales at various spatial scales (Betzel and Bassett, 2017; Hansen et al., 2022; Keller et al., 2023; Markello et al., 2022; Sydnor et al., 2021). Nevertheless, the consistency of our findings with previous investigations gives us confidence in the assessment that the uni-to-multimodal gradient best explains the chronotopy across the cortex at rest and during task.

4.2. *Resting-state timescales relate to all organizational schemes*

Our second major finding concerns the resting-state timescales. We

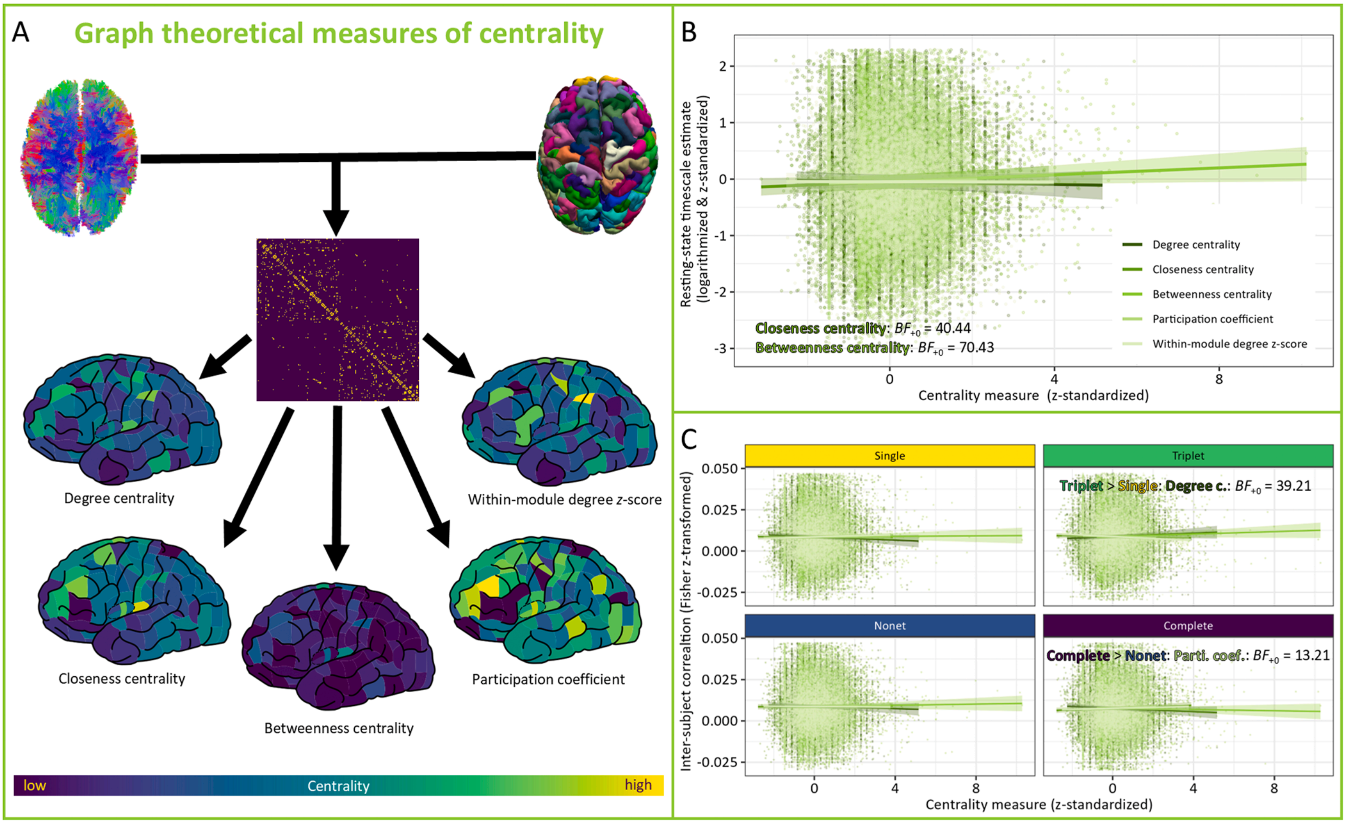

Fig. 8. Methods for extraction and results of intrinsic resting-state timescale and inter-subject correlation analyses for the graph theoretical measures of network centrality.

Note. (A) Individual nodal measures of centrality were calculated for each of the 219 nodes. We considered degree centrality, closeness centrality, betweenness centrality, participation coefficient and within-module degree *z*-score. (B) Fixed effect predictions of all investigated graph measures of centrality with 95 % credibility interval marked. (C) Plots are arranged according to Condition. Fixed effect predictions of all investigated graph measures of centrality with 95 % credibility interval marked. Degree c. = Degree centrality, Parti. coef. = Participation coefficient, BF = Bayes factor.

hypothesized for each organizational scheme that the resting-state timescales as estimated by the decay of the ACF (Raut et al., 2020) would increase, thus being slower, in hierarchically higher areas. Before discussing the individual organizational schemes, we can summarize that by and large we found this trend for all organizational schemes.

4.2.1. *Rich Club architecture*

Starting with the RC architecture, we discovered the resting-state timescales increase from Local nodes to Feeder nodes and RC hubs, while the timescales in Feeder nodes and RC hubs did not differ significantly. Thus, we could in large parts corroborate our hypothesis and replicate previous findings (Gollo et al., 2015; Senden et al., 2017). The non-significant differences between hubs and Feeder nodes could be caused by the synchronization of neighbouring nodes by the RC. As Gollo et al. (2015) described, the resonant network motifs that connect RC hubs with their direct neighbours are perfectly suited to accommodate such synchronization. Thus, our findings can be seen as further indication of this previously suggested synchronization (Aguilar-Velázquez and Guzmán-Vargas, 2019; Senden et al., 2014, 2017; Watanabe, 2013) .

4.2.2. *Diverse Club architecture*

For the DC architecture, our findings resembled those for the RC architecture and largely followed the predicted trends. DC hubs in comparison to both Local and Feeder nodes had slower intrinsic timescales. Additionally, we could find a non-significant trend for slower timescales in Feeder nodes compared with Local nodes. Thus, the results rather depict a slow increase in timescales from one level of node classification to the next. The synchronization between directly neighbouring nodes that was shown for the RC (Gollo et al., 2015) is not as prevalent in DC nodes. This finding corresponds to previous studies suggesting that the DC might be more involved in tasks rather than in synchronization (Bertolero et al., 2017; Keller et al., 2023). Thus, our resting-state results also slightly favor the RC architecture in explaining the cortical timescales in absence of a task, hinting at the importance of the RC for complex resting-state dynamics (Zamora-López et al., 2016).

4.2.3. *Rich or Diverse Club?*

The reported similarities between DC and RC architectures are likely caused by the similarity of the architectures in their classification of nodes. As our spin χ^2-test between the group-wise classifications indicated, the two architectures are highly dependent (Lee, 2016). Thus, naturally the question remains, what distinguishes RC and DC. In its initial proposal the DC was directly compared with the RC, but, in contrast to our results, no substantial overlap between DC and RC hubs was reported (Bertolero et al., 2017). Beyond that, it was suggested that the DC lays at a lower level in the cortical hierarchy than the RC (Keller et al., 2023). However, we used a refined identification of the RC hubs (Mecklenbrauck et al., 2024; Riedel et al., 2022) in this study that not only adheres closer to the original definition of RC (Colizza et al., 2006) but also uses multiple combined measures of the RC regime and centrality as previously recommended (van den Heuvel and Sporns, 2013a). This differed from the definition in Bertolero et al. (2017) that used a nodal strength cutoff. The overlap between DC and RC thereby will certainly also be influenced by the inclusion of the participation coefficient as well as other centrality measures that focus more on efficiency and communication (Hagmann et al., 2008; Jung et al., 2017) in our definition of RC. Furthermore, we also adjusted the classification of the

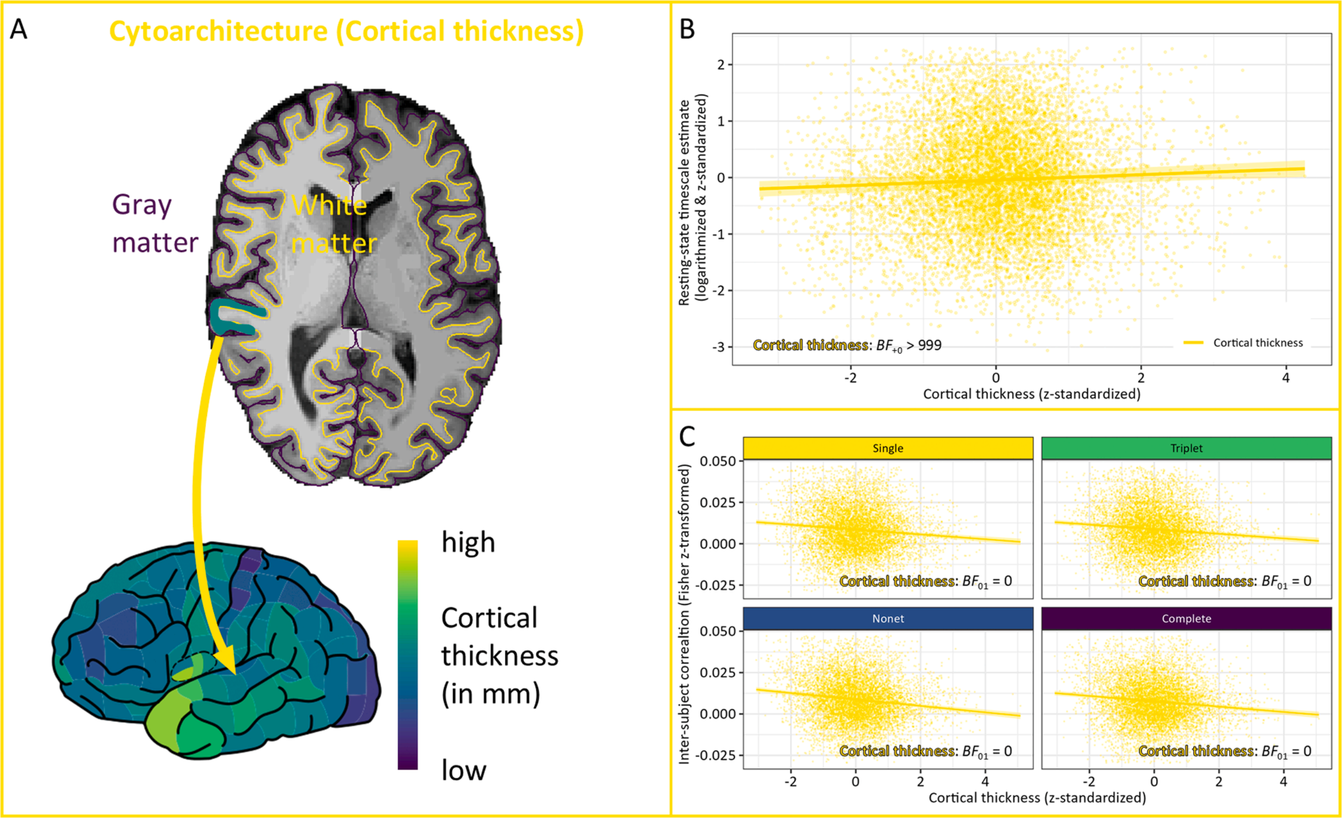

Fig. 9. Methods for extraction and results of intrinsic resting-state timescale and inter-subject correlation analyses for cortical thickness as an approximation of cytoarchitectural differences.

Note. (A) Cortical thickness can be used as an approximation for cytoarchitectural differences (Wagstyl et al., 2015). It was calculated as the average distance between the gray matter and white matter for each parcel (Goto et al., 2022). (B) Fixed effect prediction of cortical thickness as approximation of cytoarchitectural differences with 95 % credibility interval marked. (C) Plots are arranged according to CONDITION. Fixed effect prediction of cortical thickness as approximation of cytoarchitectural differences with 95 % credibility interval marked. BF = Bayes factor.

Table 1

Comparison of $\widehat{\text{elpd}}_{\text{loo}}$ of the models for the investigated organizational schemes in the intrinsic resting-state timescale analysis.

Organizational scheme	$\widehat{\text{elpd}}_{\text{loo}}$	$se(\widehat{\text{elpd}}_{\text{loo}})$	$\widehat{\text{elpd}}_{\text{diff}}$	$se\left(\widehat{\text{elpd}}_{\text{diff}}\right)$
Uni-to-multimodal gradient (Ji atlas)	−11789.63	69.01	0.00	0.00
Posterior/lateral-to-anterior/medial gradient	−11808.58	68.92	−18.95	10.77
Uni-to-multimodal gradient (SFC)	−11843.28	68.89	−53.65	13.93
Graph measures of centrality	−11852.35	68.84	−62.71	13.16
Cytoarchitecture (Cortical thickness)	−11854.55	68.84	−64.92	10.99
Rich Club architecture	−11866.26	68.82	−76.63	12.33
Null model/No scheme	−11866.79	68.79	−77.16	12.38
Diverse Club architecture	−11866.89	68.80	−77.26	12.36

Note. Models are considered to be better if the absolute elpd_{loo} difference is larger than one standard error (Mohor et al., 2021). $\widehat{\text{elpd}}_{\text{loo}}$ = expected log pointwise predictive density for a new dataset calculated using Pareto smoothed importance sampling leave-one-out-cross-validation (PSIS-LOO-CV), $\widehat{\text{elpd}}_{\text{diff}}$ = difference between the $\widehat{\text{elpd}}_{\text{loo}}$ of a model and the best performing model, *se* = standard error of the variable, SFC = Stepwise functional connectivity.

DC hubs according to the original definition of clubness (Colizza et al., 2006) but still based the identification of candidate hubs just on the participation coefficient, as proposed by Bertolero et al. (2017). However, the exclusive usage of the participation coefficient to identify hubs has recently been questioned as it could lead to misleading results if not carefully controlled (Oldham and Fornito, 2023). Nevertheless, the participation coefficient in general captures additional information about the centrality of a node other measures do not contain (Oldham et al., 2019). Recent results have even shown that RC and DC can capture complementary properties of the network (Lohia et al., 2024; Xue et al., 2020). Ultimately, more research and a revised and standardized definition of RC and especially DC are necessary to settle the debate between the RC and DC architectures.

4.2.4. *Uni-to-multimodal gradient*

As discussed in detail in Section 4.1, we used two approaches that

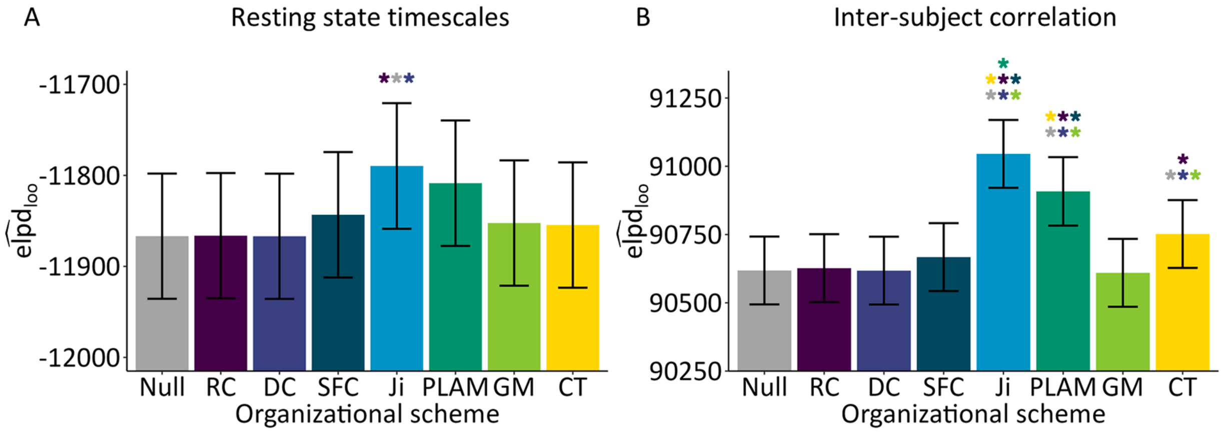

Fig. 10. Results of Bayesian model comparison.

Note. (A) Model comparison for resting-state timescale analysis. (B) Model comparison for Inter-subject correlation analysis. $\widehat{\text{elpd}}_{\text{loo}}$ = expected log pointwise predictive density for new dataset using Pareto smoothed importance sampling leave-one-out-cross-validation criterion; Null = Null model (no organizational scheme); RC = Rich Club architecture; DC = Diverse Club architecture; SFC = Uni-to-multimodal gradient (stepwise functional connectivity); Ji = Uni-to-multimodal gradient (Ji atlas classification); PLAM = Posterior/lateral-to-anterior/medial gradient; GM = Graph measures of centrality; CT = Cytoarchitecture (cortical thickness); * model has significantly higher $\widehat{\text{elpd}}_{\text{loo}}$ than models coded in respective color.

Table 2

Comparison of $\widehat{\text{elpd}}_{\text{loo}}$ of the models for the investigated organizational schemes in the inter-subject correlation analysis.

Organizational scheme	$\widehat{\text{elpd}}_{\text{loo}}$	$se(\widehat{\text{elpd}}_{\text{loo}})$	$\widehat{\text{elpd}}_{\text{diff}}$	$se\left(\widehat{\text{elpd}}_{\text{diff}}\right)$
Uni-to-multimodal gradient (Ji atlas)	91045.48	124.18	0.00	0.00
Posterior/lateral-to-anterior/medial gradient	90908.07	125.30	−137.41	28.04
Cytoarchitecture (Cortical thickness)	90752.00	124.14	−293.48	25.85
Uni-to-multimodal gradient (SFC)	90667.29	124.37	−378.19	30.19
Rich Club architecture	90626.95	124.32	−418.53	30.00
Null model/No scheme	90618.35	124.25	−427.13	29.58
Diverse Club architecture	90617.87	124.27	−427.61	29.93
Graph measures of centrality	90609.78	124.28	−435.70	30.31

Note. Models are considered to be better if the absolute elpd_{loo} difference is larger than one standard error (Mohor et al., 2021). $\widehat{\text{elpd}}_{\text{loo}}$ = expected log pointwise predictive density for a new dataset calculated using Pareto smoothed importance sampling leave-one-out-cross-validation (PSIS-LOO-CV), $\widehat{\text{elpd}}_{\text{diff}}$ = difference between the $\widehat{\text{elpd}}_{\text{loo}}$ of a model and the best performing model, *se* = standard error of the variable, SFC = Stepwise functional connectivity.

address the multimodality as a continuous measure very differently. The uni-to-multimodal gradient was firstly determined by the difference between the SFC pattern at the seventh and the first link-step and secondly by the multimodality percentage based on the overlap between the Ji atlas (Ji et al., 2019) and the applied lausanne250 parcellation (Cammoun et al., 2012). Even though we used two different continuous approaches in modelling multimodality we were able to replicate findings that used dichotomous classification of uni- and multimodal cortices (Golesorkhi et al., 2021a; Ito et al., 2020). Both modelling approaches produced the expected, similar results, predicting an increase of the resting-state timescales with the multimodality of an area.

4.2.5. *Posterior/lateral-to-anterior/medial gradient*

We found an increase of the resting-state timescales from posterior to anterior areas, mirroring the results observed for cortical peak frequencies (Mahjoory et al., 2020). Against our prediction, we were not able to find a general increase of timescales towards more medial regions. However, we did find the predicted significant interaction between the poster-to-anterior and lateral-to-medial trends, suggesting that the lateral-to-medial trend is specifically focused to the frontal lobe. Indeed, we included the posterior/lateral-to-anterior/medial gradient because it is a part of many classic theories of cortical control which mainly concern the frontal lobe (Badre and D'Esposito, 2009; Badre and Nee, 2018; Fuster, 2001; Ingvar, 1985; Koechlin and Summerfield, 2007). Notably, in their proposal of an additional medial trend Alexander and Brown (2018) also focused on the frontal lobe. Thus, it seems plausible that we found an interaction effect identifying slower timescales not more medial in general but especially when moving towards frontal areas of the brain. Based on these theoretical, but also structural and functional findings, there is considerable evidence that medial-frontal areas are involved in higher levels of cognitive processing (Alexander and Brown, 2018; Badre and Nee, 2018; Chanes and Feldman Barrett, 2016; Jobson et al., 2021).

4.2.6. *Graph measures of centrality*

Since previous studies reported the relationship between nodal measures of centrality and the chronotopy (Fallon et al., 2020; Lurie et al., 2024; Sethi et al., 2017) we also explored how the graph measures we used as hub scores in the RC identification (also see Mecklenbrauck et al., 2024; Riedel et al., 2022) faired in explaining the differences in resting-state timescales. We found significantly slower resting-state timescales with an increasing betweenness centrality and increasing closeness centrality as well as a non-significant positive trend between timescales and the participation coefficient of a node. Our results thus extend upon previous findings which reported on relationships for degree centrality (Fallon et al., 2020; Lurie et al., 2024; Sethi et al., 2017) as well as the participation coefficient and within module degree *z*-score (Lurie et al., 2024) but did not consider the betweenness and closeness centralities. Modelling all five measures together, we could however not replicate all these previous findings. One possible explanation for this is the high correlation between the measures of centrality (Oldham et al., 2019) we also showed in the spin test using the group average scores. Since we combined all fives measures into a single model, overlap in the proportions of explained variance could be a reason for replicating previous results. However, we examined all models for issues with multicollinearity and did not identify any violations (Wooldridge, 2013). Still, especially betweenness and closeness centrality describe similar concepts as both indicate nodes that are important for short paths in the network (Rubinov and Sporns, 2010) and characterize important integrative hubs (Bassett et al., 2008; de Reus and van den Heuvel, 2013; Hagmann et al., 2008; Harriger et al., 2012; Jung et al., 2017; Sepulcre et al., 2010; Whitaker et al., 2016). Moreover, a recent study showed that both betweenness and closeness centrality negatively related to the complexity of the signal in task and at rest, which can be interpreted as a less diverse activity in these nodes (Neudorf et al., 2020), thus is comparable to the higher autocorrelation, i.e., slower timescales we found for both centrality measures. Hence, our results could also imply that highly integrative nodes display slower rhythms. Beyond that, there are many more centrality measures (Oldham et al., 2019) indicative of important nodes (i.e., Katz centrality; Fletcher and Wennekers, 2018). Thus, based on our and other previous results, future research might be inclined to explore more relationships between timescales and different centrality measures, especially since it was already shown for betweenness centrality that variation in centrality measures can be used as a biomarker (Bassett et al., 2008).

4.2.7. *Cortical thickness*

Lastly, we also explored the relationship between cytoarchitecture approximated by cortical thickness and the intrinsic timescales. Previous studies revealed that areas higher up the cortical hierarchy have a less laminar pattern but a higher cortical thickness (Chanes and Feldman Barrett, 2016; Saberi et al., 2023; Wagstyl et al., 2015). Accordingly, we found that the resting-state timescales increased with a higher cortical thickness, replicating previous findings (Gao et al., 2020). It should be noted that the detected relation of the cortical thickness and the cortical chronotopy strongly depends on the selected parcellation scheme of the cortex, as the cytoarchitectural differences do not follow gyral and sulcal boarders (Amunts et al., 2007). This is critical since the applied parcellation scheme, lausanne250, is based on the structural margins of the Desikan-Killiany atlas (Cammoun et al., 2012; Desikan et al., 2006). Thus, a future deeper investigation of the relation between cytoarchitecture and the temporal scales of the cortex will require a parcellation based on the cortical microstructure (e.g., Amunts et al., 2020).

4.2.8. *Summary of resting-state timescale results*

To summarize, we found evidence for the relationship of different organizational schemes and structural features with the intrinsic cortical timescales as estimated by the decay of the ACF (Raut et al., 2020). Since we could corroborate nearly all our hypotheses for the resting-state analysis and replicated many previous findings, the question remains how distinct the investigated organizational schemes are. While we explored the relationships amongst the organizational schemes using spin tests (Alexander-Bloch et al., 2018) and found significant relationships between the RC and DC architectures and expectedly between the two approaches to the uni-to-multimodal gradient and the different centrality measures, previous studies revealed additional, significant coherence between several of the here examined features. For instance, a higher cortical thickness was previously related to multimodal cortices (Burt et al., 2018; Wagstyl et al., 2015) and RC hubs (Scholtens et al., 2014; van den Heuvel et al., 2015). Just based on their definitions, multimodal cortices and RC hubs describe largely overlapping concepts (van den Heuvel and Sporns, 2013b; Zamora-López et al., 2011) as both organizational patters are proposed to integrate information across different functional networks (Chaudhuri et al., 2015; van den Heuvel and Sporns, 2013b, 2013a; Yeo et al., 2015; Zamora-López et al., 2009, 2010). Therefore, it comes to no surprise that the uni-to-multimodality gradient and the RC architecture are used rather synonymously (e.g., Golesorkhi et al., 2021a; Ji et al., 2019; Murphy et al., 2019). These two patterns thus could describe a functional and a structural view on the same question. Possible remaining differences between them could relate to the decoupling of functional and structural features in higher cortical areas (Liu et al., 2023; Preti and Van De Ville, 2019; Vázquez-Rodríguez et al., 2019). Furthermore, the RC also is mainly found within midline areas (van den Heuvel and Sporns, 2011) which could explain an overlap with the spatial posterior/lateral-to-anterior/medial gradient, even though RC hubs are usually found in both frontal and parietal areas (e.g., Mecklenbrauck et al., 2024; Riedel et al., 2022).

To conclude, while we did not find a complete overlap between the investigated organizational schemes, they are certainly not independent of each other. Thus, a promising future avenue could focus on the integration of multiple descriptions of cortical hierarchy into a single gradient or classification index across imaging modalities and methods. Recent studies provide positive preliminary evidence for this approach (Hansen et al., 2022; Shafiei et al., 2023; Sydnor et al., 2021).

4.3. *Task effects*

We hypothesized that areas higher in the cortical hierarchy should demonstrate larger ISC values in conditions that contain hierarchically higher, temporally more persistent structures in the stimuli, as these areas with longer TRWs should be engaged specifically by more persistent stimuli (e.g., Hasson et al., 2004). We found that the ISC values in all four experimental conditions (Single, Triplet, Nonet and Complete) reduced with higher multimodality in the Ji atlas-based model and in all but the Nonet condition in the SFC-based model. Also, for thicker areas in the cortical thickness model the ISC values decreased, which is further indication for the relationship between these two organizational schemes (Burt et al., 2018; Wagstyl et al., 2015). This decrease of ISC towards hierarchically higher areas can be explained by the less stimulus-determined processes (Ren et al., 2017; Schmälzle et al., 2017) and more diverse functions in these regions (Cui et al., 2020). When comparing the effects between experimental conditions we found the predicted increase in the effect of multimodality on the ISC values between the Single and Triplet condition for both approaches of the uni-to-multimodal gradient as well as between the Nonet and Triplet conditions for just the SFC model. Similarly, the posterior-to-anterior gradient was significantly more pronounced in the Triplet condition compared to the Single condition. The lateral-to-medial gradient as well as the interaction of the posterior-to-anterior and lateral-to-medial gradients however were more pronounced in the Nonet as compared to the Triplet condition. This could imply the additional engagement of higher order areas in in medial and especially anterior-medial cortex, thus providing evidence for the tuning of higher order areas being to temporally more persistent structures in the stimulus (e.g., Aberbach--Goodman and Mukamel, 2023; Farbood et al., 2015; Hasson et al., 2015; Lerner et al., 2011). These results also match our previous findings of a posterior-to-anterior trend for processing hierarchically higher levels of the stimulus (Mecklenbrauck et al., 2024). Additionally, the Triplet compared to the Single condition exhibited a larger effect of degree centrality on the ISC values. Further, the effect of the participation coefficient was larger in the Complete compared to the Nonet condition. These two findings might conform to previous findings showing that highly connected nodes are essential for integrating stimuli (Fallon et al., 2020) while especially diverse nodes that connect between different modules of the network are more involved in integrative tasks (Bertolero et al., 2017; Keller et al., 2023; Lurie et al., 2024). However, looking at the credibility intervals of the effects across models revealed that specifically the Triplet condition behaved distinctly from all the other experimental conditions, even though the four conditions were incrementally nested. This inconsistency demands caution with the presented interpretations.

Beyond that, the applied paradigm might have restrained our ability to identify consistent task results across the organizational schemes: Firstly, the ISC values that were calculated based on task data using the hierarchically nested but abstract digit sequences were much lower than in paradigms using more complex, naturalistic stimuli (e.g., Schmälzle et al., 2017). Controllable, abstract stimuli are the standard in neuroscience (Rust and Movshon, 2005). However, the choice of control over ecological validity might have limited a reliable and widespread activation in multimodal areas (Hasson et al., 2010; Sonkusare et al., 2019).

Secondly, in deviation to other ISC studies (e.g., Lerner et al., 2011) we included a task in our paradigm. Hierarchically nested sequences of stimuli can be chunked into bigger units to make full use of working memory capacity (Mathy and Feldman, 2012). Chunking however requires attention to the stimulus to provoke a global activation of hierarchically higher cortical areas (Dehaene et al., 2015; Mashour et al., 2020). The addition of a visual task might have prevented the necessary attention to the sequence, thus impeding the ignition of higher order areas (Bekinschtein et al., 2009). Finding correlations across participants could then have been further restricted by the more diverse activity in these higher order areas (Cui et al., 2020; Ren et al., 2017; Schmälzle et al., 2017).

4.4. Limitations

In addition to the task paradigm, there are a few other limitations to consider. As stated above, the relation between the chronotopy of the cortex and its features is dependent of the applied parcellation scheme (Amunts et al., 2007). Previous studies further found that the choice of parcellation scheme has a large effect on the appearance of cortical network as a whole (Bassett et al., 2011; Bryce et al., 2021; Cammoun et al., 2012; Qi et al., 2015; Seguin et al., 2020; Sporns, 2011). As most of the investigated organizational schemes were derived from structural and functional networks, our choice for the Lausanne parcellation scheme with 219 cortical parcels certainly had an impact on the results. We specifically selected this parcellation scheme since it was the most reliable (Cammoun et al., 2012) and neuroanatomically valid (Amunts and Zilles, 2015) parcellation scheme of the ones available in the CATO toolbox (de Lange et al., 2023) we applied for network reconstruction. However, the Lausanne parcellation scheme is not without its limitations. Firstly, as a sub-parcellation of the Desikan-Killiany atlas (Desikan et al., 2006) it follows gyral and sulcal boundaries, which not all features adhere to (Amunts et al., 2007). Secondly, the sub-parcellation was done by dividing each original parcel in a set of equally sized smaller parcels to achieve a voxel-level resolution. This procedure is rather arbitrary, and its anatomical validity is questionable (Qi et al., 2015). There is a multitude of possible parcellations of the human brain (Eickhoff et al., 2018) making use of only anatomical (Desikan et al., 2006; Destrieux et al., 2010; Tzourio-Mazoyer et al., 2002) or only functional guidelines (Craddock et al., 2012; Gordon et al., 2016; Schaefer et al., 2018; Shen et al., 2013) or also combining multiple sources of data (Fan et al., 2016; Glasser et al., 2016). Finding the appropriate parcellation scheme might be more dependent on the research question (Schaefer et al., 2018). Faced with this arbitrariness, it can be a common approach to compare the results across different parcellation schemes (e.g., Riedel et al., 2022). We have not included this option in the scope of this paper, which is a limitation. However, the consistency of our main finding that the uni-to-multimodal gradient shapes the cortical chronotopy with previous studies using various other parcellation schemes (Gao et al., 2020; Golesorkhi et al., 2021a; Ito et al., 2020; Raut et al., 2020) gives us sufficient confidence in this result.

We also have to mention the data quality of the DWI data, that did not follow current recommendations (Jones et al., 2013). Consequently, we had to exclude subcortical areas from the analysis, even though the cortical hierarchy was found to extend also to the subcortex (Alexander et al., 1986; Badre and Nee, 2018; Siegle et al., 2021). Recent studies even found a variation of timescales in subcortical areas that mirror that of the cortex (Raut et al., 2020) and indicated that the thalamus plays a crucial role in shaping functional dynamics (Harris et al., 2019; Müller et al., 2020; Shine et al., 2019). However, despite using a combined DTI and GQI algorithm that performed the best in distinguishing crossing and kissing fibres (de Lange et al., 2023), the available data would have limited the interpretability of results from the subcortex (Kai et al., 2022). The limited data quality also led to our decision to binarize the structural connectivity matrices since weighted connectivity measure might be biased (Calamante, 2019; Fornito et al., 2016). Given an improved data quality, future research could therefore make use of the entire variability of weighted network measures (Fornito et al., 2016) and also consider the previously found role of the subcortex in processing hierarchically nested stimuli (Graybiel, 2008).

5. Conclusion

To conclude, we investigated the effect of six cortical organizational schemes and features on the intrinsic resting-state timescales and the ISC values from a task that presented participants with a hierarchically nested stimulus sequence of increasing temporal persistency. In both cases, the uni-to-multimodal gradient, as determined by an atlas classification, proved to be the best fitting model. In addition, we provide further evidence for the relationship between the intrinsic timescales and the functional hierarchy of the cortex, the network structure of the human connectome as well as cytoarchitectural properties of an area, corroborating previous results. Future studies investigating the brain's microstructural organization are needed to gain deeper insights into how exactly the uni-to-multimodal gradient shapes the cortex's chronotopy and how different organizational schemes interrelate.

Ethics statement

This study was conducted in accordance with the Declaration of Helsinki and approved by the Local Ethics Committee of the University of Münster. Participants signed an informed consent before participation.

Funding

The authors received no specific funding for this work.

CRediT authorship contribution statement

Falko Mecklenbrauck: Writing – review & editing, Writing – original draft, Visualization, Software, Project administration, Methodology, Investigation, Formal analysis, Data curation, Conceptualization. **Jorge Sepulcre:** Software, Methodology. **Jana Fehring:** Writing – review & editing, Software, Methodology. **Ricarda I. Schubotz:** Writing – review & editing, Writing – original draft, Supervision, Resources, Project administration, Methodology, Funding acquisition.

Declaration of competing interest

The authors declare that they have no conflict of interest.

Acknowledgement

The authors thank Monika Mertens and Lena M. Puder for their help during data collection, Lena M. Puder, Simon Wieczorek, and Maria L. Hofmann for help in the quality control process, Kristin Stroop and Simon Wieczorek for help in testing the paradigm, and Sophie Siestrup for helpful comments on the manuscript.

Supplementary materials

Supplementary material associated with this article can be found, in the online version, at doi:10.1016/j.neuroimage.2024.120914.

Data availability

All code, one exemplary, minimally processed participant and data sets to replicate the main analyses are available at https://github.com/FalkMeck/Decoding_Cortical_Chronotopy.git

References

Aberbach-Goodman, S., Mukamel, R., 2023. Temporal hierarchy of observed goal-directed actions. Sci. Rep. 13 (1), 1–13. https://doi.org/10.1038/s41598-023-46917-z.

Agcaoglu, O., Wilson, T.W., Wang, Y.P., Stephen, J., Calhoun, V.D., 2019. Resting state connectivity differences in eyes open versus eyes closed conditions. Hum. Brain Mapp. 40 (8), 2488–2498. https://doi.org/10.1002/hbm.24539.

Aguilar-Velázquez, D., Guzmán-Vargas, L., 2019. Critical synchronization and 1/f noise in inhibitory/excitatory rich-club neural networks. Sci. Rep. 9 (1), 1–13. https://doi.org/10.1038/s41598-018-37920-w.

Aguirre, G.K., Mattar, M.G., Magis-Weinberg, L., 2011. De Bruijn cycles for neural decoding. Neuroimage 56 (3), 1293–1300. https://doi.org/10.1016/j.neuroimage.2011.02.005.

Alexander, G.E., DeLong, M.R., Strick, P.L., 1986. Parallel organization of functionally segregated circuits linking basal ganglia and cortex. Annu. Rev. Neurosci. 9, 357–381. https://doi.org/10.1146/annurev.ne.09.030186.002041.

Alexander, W.H., Brown, J.W., 2018. Frontal cortex function as derived from hierarchical predictive coding. Sci. Rep. 8 (1), 1–11. https://doi.org/10.1038/s41598-018-21407-9.

Alexander-Bloch, A.F., Shou, H., Liu, S., Satterthwaite, T.D., Glahn, D.C., Shinohara, R.T., Vandekar, S.N., Raznahan, A., 2018. On testing for spatial correspondence between maps of human brain structure and function. Neuroimage 178 (February), 540–551. https://doi.org/10.1016/j.neuroimage.2018.05.070.

Alston, C., Kuhnert, P., Low Choy, S., Mcvinish, R., Mengersen, K., Choy, S.L., Mcvinish, R., Mengersen, K., 2004. Bayesian model comparison: review and discussion. In: ISI 2005: the 55th Session of the International Statistical Institute, Sydney, 2005, pp. 1–4. http://iase-web.org/documents/papers/isi55/Alston-Kuhnert-Low_Choy-McVinish-Mengersen.pdf.

Amunts, K., Mohlberg, H., Bludau, S., Zilles, K., 2020. Julich-brain: a 3D probabilistic atlas of the human brain's cytoarchitecture. Science 369 (6506), 988–992. https://doi.org/10.1126/science.abb4588.

Amunts, K., Schleicher, A., Zilles, K., 2007. Cytoarchitecture of the cerebral cortex-more than localization. Neuroimage 37 (4), 1061–1065. https://doi.org/10.1016/j.neuroimage.2007.02.037.

Amunts, K., Zilles, K., 2015. Architectonic mapping of the human brain beyond brodmann. Neuron 88 (6), 1086–1107. https://doi.org/10.1016/j.neuron.2015.12.001.

Andersson, J.L.R., Skare, S., Ashburner, J., 2003. How to correct susceptibility distortions in spin-echo echo-planar images: application to diffusion tensor imaging. Neuroimage 20 (2), 870–888. https://doi.org/10.1016/S1053-8119(03)00336-7.

Andersson, J.L.R., Sotiropoulos, S.N., 2016. An integrated approach to correction for off-resonance effects and subject movement in diffusion MR imaging. Neuroimage 125, 1063–1078. https://doi.org/10.1016/j.neuroimage.2015.10.019.

Badre, D., D'Esposito, M., 2009. Is the rostro-caudal axis of the frontal lobe hierarchical? Nat. Rev. Neurosci. 10 (9), 659–669. https://doi.org/10.1038/nrn2667.

Badre, D., Nee, D.E., 2018. Frontal cortex and the hierarchical control of behavior. Trends Cogn. Sci. 22 (2), 170–188. https://doi.org/10.1016/j.tics.2017.11.005. Elsevier Ltd.

Baldassano, C., Chen, J., Zadbood, A., Pillow, J.W., Hasson, U., Norman, K.A., 2017. Discovering event structure in continuous narrative perception and memory. Neuron 95 (3), 709–721.e5. https://doi.org/10.1016/j.neuron.2017.06.041.

Bassett, D.S., Brown, J.A., Deshpande, V., Carlson, J.M., Grafton, S.T., 2011. Conserved and variable architecture of human white matter connectivity. Neuroimage 54 (2), 1262–1279. https://doi.org/10.1016/j.neuroimage.2010.09.006.

Bassett, D.S., Bullmore, E., Verchinski, B.A., Mattay, V.S., Weinberger, D.R., Meyer-Lindenberg, A., 2008. Hierarchical organization of human cortical networks in health and schizophrenia. J. Neurosci. 28 (37), 9239–9248. https://doi.org/10.1523/JNEUROSCI.1929-08.2008.

Behzadi, Y., Restom, K., Liau, J., Liu, T.T., 2007. A component based noise correction method (CompCor) for BOLD and perfusion based fMRI. Neuroimage 37 (1), 90–101. https://doi.org/10.1016/j.neuroimage.2007.04.042.

Bekinschtein, T.A., Dehaene, S., Rohaut, B., Tadel, F., Cohen, L., Naccache, L., 2009. Neural signature of the conscious processing of auditory regularities. Proc. Natl. Acad. Sci. USA 106 (5), 1672–1677. https://doi.org/10.1073/pnas.0809667106.

Benjamini, Y., Hochberg, Y., 1995. Controlling the false discovery rate : a practical and powerful approach to multiple testing. *J. R. Stat. Soc.* Ser. B (Methodological) 57 (1), 289–300.

Bertolero, M.A., Yeo, B.T.T., D'Esposito, M., 2017. The diverse club. Nat. Commun. 8 (1), 1–10. https://doi.org/10.1038/s41467-017-01189-w.

Betzel, R.F., Bassett, D.S., 2017. Multi-scale brain networks. Neuroimage 160 (November 2016), 73–83. https://doi.org/10.1016/j.neuroimage.2016.11.006.

Blondel, V.D., Guillaume, J.L., Lambiotte, R., Lefebvre, E., 2008. Fast unfolding of communities in large networks. J. Stat. Mech. 2008 (10), 1–12. https://doi.org/10.1088/1742-5468/2008/10/P10008.

Bond, C.F., Richardson, K., 2004. Seeing the Fisher Z-transformation. Psychometrika 69 (2), 291–303. https://doi.org/10.1007/BF02295945.

Brimijoin, W.O., O'Neill, W.E., 2010. Patterned tone sequences reveal non-linear interactions in auditory spectrotemporal receptive fields in the inferior colliculus. Hear. Res. 267 (1–2), 96–110. https://doi.org/10.1016/j.heares.2010.04.005.

Brown, J.A., Terashima, K.H., Burggren, A.C., Ercoli, L.M., Miller, K.J., Small, G.W., Bookheimer, S.Y., 2011. Brain network local interconnectivity loss in aging APOE-4 allele carriers. Proc. Natl. Acad. Sci. USA 108 (51), 20760–20765. https://doi.org/10.1073/pnas.1109038108.

Bryce, N.V., Flournoy, J.C., Guassi Moreira, J.F., Rosen, M.L., Sambook, K.A., Mair, P., McLaughlin, K.A., 2021. Brain parcellation selection: an overlooked decision point with meaningful effects on individual differences in resting-state functional connectivity. Neuroimage 243 (March), 118487. https://doi.org/10.1016/j.neuroimage.2021.118487.

Brysbaert, M., 1995. Arabic number reading: on the nature of the numerical scale and the origin of phonological recoding. J. Exp. Psychol. 124 (4), 434–452. https://doi.org/10.1037/0096-3445.124.4.434.

Bueichekú, E., Aznárez-Sanado, M., Diez, I., Uquillas, F.d.O., Ortiz-Terán, L., Qureshi, A. Y., Suñol, M., Basaia, S., Ortiz-Terán, E., Pastor, M.A., Sepulcre, J., 2020. Central neurogenetic signatures of the visuomotor integration system. Proc. Natl. Acad. Sci. USA 117 (12), 6836–6843. https://doi.org/10.1073/pnas.1912429117.

Bürkner, P.C., 2017. brms: An R package for Bayesian multilevel models using Stan. J. Stat. Softw. 80 (1). https://doi.org/10.18637/jss.v080.i01.

Bürkner, P.C. (2018). *Is the evidence ratio for a one sided hypothesis equivalent to a one sided bayes factor?* https://github.com/paul-buerkner/brms/issues/311.

Burt, J.B., Demirtaş, M., Eckner, W.J., Navejar, N.M., Ji, J.L., Martin, W.J., Bernacchia, A., Anticevic, A., Murray, J.D., 2018. Hierarchy of transcriptomic specialization across human cortex captured by structural neuroimaging topography. Nat. Neurosci. 21 (9), 1251–1259. https://doi.org/10.1038/s41593-018-0195-0.

Buxton, R.B., 2009. Introduction to Functional Magnetic Resonance Imaging. Cambridge University Press. https://doi.org/10.1017/CBO9780511605505.

Caballero-Gaudes, C., Reynolds, R.C., 2017. Methods for cleaning the BOLD fMRI signal. Neuroimage 154 (December 2016), 128–149. https://doi.org/10.1016/j.neuroimage.2016.12.018.

Calamante, F., 2019. The seven deadly sins of measuring brain structural connectivity using diffusion MRI streamlines fibre-tracking. Diagnostics 9 (3). https://doi.org/10.3390/diagnostics9030115.

Cammoun, L., Gigandet, X., Meskaldji, D., Thiran, J.P., Sporns, O., Do, K.Q., Maeder, P., Meuli, R., Hagmann, P., 2012. Mapping the human connectome at multiple scales with diffusion spectrum MRI. J. Neurosci. Methods 203 (2), 386–397. https://doi.org/10.1016/j.jneumeth.2011.09.031.

Cavanagh, S.E., Hunt, L.T., Kennerley, S.W., 2020. A diversity of intrinsic timescales underlie neural computations. Front. Neural Circuits 14 (December), 1–18. https://doi.org/10.3389/fncir.2020.615626.

Chanes, L., Feldman Barrett, L., 2016. Redefining the role of limbic areas in cortical processing. Trends Cogn. Sci. 20 (2), 96–106. https://doi.org/10.1016/j.tics.2015.11.005.

Chang, L.-C., Jones, D.K., Pierpaoli, C., 2005. RESTORE: robust estimation of tensors by outlier rejection. Magn. Reson. Med. 53 (5), 1088–1095. https://doi.org/10.1002/mrm.20426.

Chang, L.-C., Walker, L., Pierpaoli, C., 2012. Informed RESTORE: a method for robust estimation of diffusion tensor from low redundancy datasets in the presence of physiological noise artifacts. Magn. Reson. Med. 68 (5), 1654–1663. https://doi.org/10.1002/mrm.24173.

Chaudhuri, R., Knoblauch, K., Gariel, M.A., Kennedy, H., Wang, X.J., 2015. A large-scale circuit mechanism for hierarchical dynamical processing in the primate cortex. Neuron 88 (2), 419–431. https://doi.org/10.1016/j.neuron.2015.09.008.

Chen, J., Hasson, U., Honey, C.J., 2015. Processing timescales as an organizing principle for primate cortex. Neuron 88 (2), 244–246. https://doi.org/10.1016/j.neuron.2015.10.010.

Ciric, R., Wolf, D.H., Power, J.D., Roalf, D.R., Baum, G.L., Ruparel, K., Shinohara, R.T., Elliott, M.A., Eickhoff, S.B., Davatzikos, C., Gur, R.C., Gur, R.E., Bassett, D.S., Satterthwaite, T.D., 2017. Benchmarking of participant-level confound regression strategies for the control of motion artifact in studies of functional connectivity. Neuroimage 154 (March), 174–187. https://doi.org/10.1016/j.neuroimage.2017.03.020.

Colizza, V., Flammini, A., Serrano, M.A., Vespignani, A., 2006. Detecting rich-club ordering in complex networks. Nat. Phys. 2 (2), 110–115. https://doi.org/10.1038/nphys209.

Corbin, N., Todd, N., Friston, K.J., Callaghan, M.F., 2018. Accurate modeling of temporal correlations in rapidly sampled fMRI time series. Hum. Brain Mapp. 39 (10), 3884–3897. https://doi.org/10.1002/hbm.24218.

Craddock, R.C., James, G.A., Holtzheimer, P.E., Hu, X.P., Mayberg, H.S., 2012. A whole brain fMRI atlas generated via spatially constrained spectral clustering. Hum. Brain Mapp. 33 (8), 1914–1928. https://doi.org/10.1002/hbm.21333.

Cui, Z., Li, H., Xia, C.H., Larsen, B., Adebimpe, A., Baum, G.L., Cieslak, M., Gur, R.E., Gur, R.C., Moore, T.M., Oathes, D.J., Alexander-Bloch, A.F., Raznahan, A., Roalf, D. R., Shinohara, R.T., Wolf, D.H., Davatzikos, C., Bassett, D.S., Fair, D.A., Satterthwaite, T.D., 2020. Individual variation in functional topography of association networks in youth. Neuron 106 (2), 340–353.e8. https://doi.org/10.1016/j.neuron.2020.01.029.

Cullen, A.C., Frey, H.C., 1999. Probabilistic Techniques in Exposure Assessment: A Handbook for Dealing with Variability and Uncertainty in Models and Inputs. Springer Science & Business.

Dale, A.M., Fischl, B., Sereno, M.I., 1999. Cortical surface-based analysis. Neuroimage 9 (2), 179–194. https://doi.org/10.1006/nimg.1998.0395.

de Bruijn, G.N., 1946. A combinatorial problem. Proc. Koninklijke Nederlandse Acad. van Wetenschappen 49, 758–764. http://ci.nii.ac.jp/naid/10019660672/en/.

de Lange, S.C., Helwegen, K., van den Heuvel, M.P., 2023. Structural and functional connectivity reconstruction with CATO—A connectivity analysis TOolbox. Neuroimage 273 (April), 120108. https://doi.org/10.1016/j.neuroimage.2023.120108.

de Reus, M.A., van den Heuvel, M.P., 2013. Rich club organization and intermodule communication in the cat connectome. J. Neurosci. 33 (32), 12929–12939. https://doi.org/10.1523/jneurosci.1448-13.2013.

Dehaene, S., 2001. Précis of the number sense. Mind Lang. 16 (1), 16–36. https://doi.org/10.1111/1468-0017.00154.

Dehaene, S., Meyniel, F., Wacongne, C., Wang, L., Pallier, C., 2015. The neural representation of sequences: from transition probabilities to algebraic patterns and linguistic trees. Neuron 88 (1), 2–19. https://doi.org/10.1016/j.neuron.2015.09.019.

Demirtaş, M., Burt, J.B., Helmer, M., Ji, J.L., Adkinson, B.D., Glasser, M.F., Van Essen, D.C., Sotiropoulos, S.N., Anticevic, A., Murray, J.D., 2019. Hierarchical heterogeneity across human cortex shapes large-scale neural dynamics. Neuron 101 (6), 1181–1194.e13. https://doi.org/10.1016/j.neuron.2019.01.017.

Desikan, R.S., Ségonne, F., Fischl, B., Quinn, B.T., Dickerson, B.C., Blacker, D., Buckner, R.L., Dale, A.M., Maguire, R.P., Hyman, B.T., Albert, M.S., Killiany, R.J., 2006. An automated labeling system for subdividing the human cerebral cortex on MRI scans into gyral based regions of interest. Neuroimage 31 (3), 968–980. https://doi.org/10.1016/j.neuroimage.2006.01.021.

Destrieux, C., Fischl, B., Dale, A., Halgren, E., 2010. Automatic parcellation of human cortical gyri and sulci using standard anatomical nomenclature. Neuroimage 53 (1), 1–15. https://doi.org/10.1016/j.neuroimage.2010.06.010.

Diez, I., Sepulcre, J., 2018. Neurogenetic profiles delineate large-scale connectivity dynamics of the human brain. Nat. Commun. 9 (1), 1–10. https://doi.org/10.1038/s41467-018-06346-3.

Duarte, R., Seeholzer, A., Zilles, K., Morrison, A., 2017. Synaptic patterning and the timescales of cortical dynamics. Curr. Opin. Neurobiol. 43 (April), 156–165. https://doi.org/10.1016/j.conb.2017.02.007.

Eickhoff, S.B., Stephan, K.E., Mohlberg, H., Grefkes, C., Fink, G.R., Amunts, K., Zilles, K., 2005. A new SPM toolbox for combining probabilistic cytoarchitectonic maps and functional imaging data. Neuroimage 25 (4), 1325–1335. https://doi.org/10.1016/j.neuroimage.2004.12.034.

Eickhoff, S.B., Yeo, B.T.T., Genon, S., 2018. Imaging-based parcellations of the human brain. Nat. Rev. Neurosci. 19 (11), 672–686. https://doi.org/10.1002/jmri.27188.

Fallon, J., Ward, P.G.D., Parkes, L., Oldham, S., Arnatkevičiūtė, A., Fornito, A., Fulcher, B.D., 2020. Timescales of spontaneous fMRI fluctuations relate to structural connectivity in the brain. Netw. Neurosci. 4 (3), 788–806. https://doi.org/10.1162/netn_a_00151.

Fan, L., Li, H., Zhuo, J., Zhang, Y., Wang, J., Chen, L., Yang, Z., Chu, C., Xie, S., Laird, A.R., Fox, P.T., Eickhoff, S.B., Yu, C., Jiang, T., 2016. The human brainnetome atlas: a new brain atlas based on connectional architecture. Cereb. Cortex 26 (8), 3508–3526. https://doi.org/10.1093/cercor/bhw157.

Farbood, M.M., Heeger, D.J., Marcus, G., Hasson, U., Lerner, Y., 2015. The neural processing of hierarchical structure in music and speech at different timescales. Front. Neurosci. 9 (APR), 1–13. https://doi.org/10.3389/fnins.2015.00157.

Fehring, J., Balestrieri, E., Focke, N.K., Dannlowski, U., Stier, C., Gross, J., 2024. Neurophysiological correlates of cortical hierarchy across the lifespan. BioRxiv Neurosci. 1–28. https://www.biorxiv.org/content/10.1101/2024.07.15.602693v1?rss=1&utm_source=researcher_app&utm_medium=referral&utm_campaign=RESR_MRKT_Researcher_inbound.

FIL Methods Group. (2017). *SPM12 Manual*. 15(3), 1–508. https://www.fil.ion.ucl.ac.uk/spm/doc/manual.pdf%0Ahttp://www.fil.ion.ucl.ac.uk/spm/.

Fischl, B., 2012. FreeSurfer. Neuroimage 62 (2), 774–781. https://doi.org/10.1016/j.neuroimage.2012.01.021.

Fletcher, J.M.K., Wennekers, T., 2018. From structure to activity: using centrality measures to predict neuronal activity. Int. J. Neural Syst. 28 (2). https://doi.org/10.1142/S0129065717500137.

Fornito, A., Zalesky, A., Bullmore, E., 2016. Fundamentals of Brain Network Analysis. Elsevier. https://doi.org/10.1016/C2012-0-06036-X.

Fuster, J.M., 2001. The prefrontal cortex—An update: time is of the essence. Neuron 30 (2), 319–333. https://doi.org/10.1016/S0896-6273(01)00285-9.

Gao, R., van den Brink, R.L., Pfeffer, T., Voytek, B., 2020. Neuronal timescales are functionally dynamic and shaped by cortical microarchitecture. Elife 9, 1–26. https://doi.org/10.7554/eLife.61277.

Gelman, A., Hwang, J., Vehtari, A., 2014. Understanding predictive information criteria for Bayesian models. Stat. Comput. 24 (6), 997–1016. https://doi.org/10.1007/s11222-013-9416-2.

Geweke, J., 2007. Bayesian model comparison and validation. Am. Econ. Rev. 97 (2), 60–64. https://doi.org/10.1257/aer.97.2.60.

Glasser, M.F., Coalson, T.S., Robinson, E.C., Hacker, C.D., Harwell, J., Yacoub, E., Ugurbil, K., Andersson, J., Beckmann, C.F., Jenkinson, M., Smith, S.M., Van Essen, D.C., 2016. A multi-modal parcellation of human cerebral cortex. Nature 536 (7615), 171–178. https://doi.org/10.1038/nature18933.

Goldman-Rakic, P.S., 1988. Topography of cognition: parallel distributed networks in primate association cortex. Annu Rev. Neurosci. 11, 137–156. https://doi.org/10.1146/annurev.ne.11.030188.001033.

Golesorkhi, M., Gomez-Pilar, J., Tumati, S., Fraser, M., Northoff, G., 2021a. Temporal hierarchy of intrinsic neural timescales converges with spatial core-periphery organization. Commun. Biol. 4 (1), 1–14. https://doi.org/10.1038/s42003-021-01785-z.

Golesorkhi, M., Gomez-Pilar, J., Zilio, F., Berberian, N., Wolff, A., Yagoub, M.C.E., Northoff, G., 2021b. The brain and its time: intrinsic neural timescales are key for input processing. Commun. Biol. 4 (1), 1–16. https://doi.org/10.1038/s42003-021-02483-6.

Gollo, L.L., Zalesky, A., Matthew Hutchison, R., van den Heuvel, M.P., Breakspear, M., 2015. Dwelling quietly in the rich club: brain network determinants of slow cortical fluctuations. Philos. Trans. R. Soc. B 370 (1668). https://doi.org/10.1098/rstb.2014.0165.

Gómez-Gardeñes, J., Zamora-López, G., Moreno, Y., Arenas, A., 2010. From modular to centralized organization of synchronization in functional areas of the cat cerebral cortex. PLoS One 5 (8). https://doi.org/10.1371/journal.pone.0012313.

Gordon, E.M., Laumann, T.O., Adeyemo, B., Huckins, J.F., Kelley, W.M., Petersen, S.E., 2016. Generation and evaluation of a cortical area parcellation from resting-state correlations. Cereb. Cortex 26 (1), 288–303. https://doi.org/10.1093/cercor/bhu239.

Gorgolewski, K.J. (2016). *MPM 1.0 asymetrical (improved reconstruction)*. https://identifiers.org/neurovault.image:29489.

Goto, M., Abe, O., Hagiwara, A., Fujita, S., Kamagata, K., Hori, M., Aoki, S., Osada, T., Konishi, S., Masutani, Y., Sakamoto, H., Sakano, Y., Kyogoku, S., Daida, H., 2022. Advantages of using both voxel-and surface-based morphometry in cortical morphology analysis: a review of various applications. Magn. Reson. Med. Sci. 21 (1), 41–57. https://doi.org/10.2463/mrms.rev.2021-0096.

Graybiel, A.M., 2008. Habits, rituals, and the evaluative brain. Annu Rev. Neurosci. 31, 359–387. https://doi.org/10.1146/annurev.neuro.29.051605.112851.

Guimerà, R., Nunes Amaral, L.A., 2005. Functional cartography of complex metabolic networks. Nature 433 (7028), 895–900. https://doi.org/10.1038/nature03288.

Hagmann, P., Cammoun, L., Gigandet, X., Meuli, R., Honey, C.J., Van Wedeen, J., Sporns, O., 2008. Mapping the structural core of human cerebral cortex. PLoS Biol. 6 (7), 1479–1493. https://doi.org/10.1371/journal.pbio.0060159.

Hansen, J.Y., Markello, R.D., Vogel, J.W., Seidlitz, J., Bzdok, D., Misic, B., 2021. Mapping gene transcription and neurocognition across human neocortex. Nat. Hum. Behav. 5 (9), 1240–1250. https://doi.org/10.1038/s41562-021-01082-z.

Hansen, J.Y., Shafiei, G., Voigt, K., Liang, E.X., Cox, S.M.L., Leyton, M., Jamadar, S.D., & Misic, B. (2022). Multimodal, multiscale connectivity blueprints of the cerebral cortex. bioRxiv, 2022.12.02.518906. https://www.biorxiv.org/content/10.1101/2022.12.02.518906v1%0Ahttps://www.biorxiv.org/content/10.1101/2022.12.02.518906v1.abstract.

Harriger, L., van den Heuvel, M.P., Sporns, O., 2012. Rich club organization of macaque cerebral cortex and its role in network communication. PLoS One 7 (9). https://doi.org/10.1371/journal.pone.0046497.

Harris, J.A., Mihalas, S., Hirokawa, K.E., Whitesell, J.D., Choi, H., Bernard, A., Bohn, P., Caldejon, S., Casal, L., Cho, A., Feiner, A., Feng, D., Gaudreault, N., Gerfen, C.R., Graddis, N., Groblewski, P.A., Henry, A.M., Ho, A., Howard, R., Zeng, H., 2019. Hierarchical organization of cortical and thalamic connectivity. Nature 575 (7781), 195–202. https://doi.org/10.1038/s41586-019-1716-z.

Hasson, U., Chen, J., Honey, C.J., 2015. Hierarchical process memory: memory as an integral component of information processing. Trends Cogn. Sci. 19 (6), 304–313. https://doi.org/10.1016/j.tics.2015.04.006.

Hasson, U., Malach, R., Heeger, D.J., 2010. Reliability of cortical activity during natural stimulation. Trends Cogn. Sci. 14 (1), 40–48. https://doi.org/10.1016/j.tics.2009.10.011.

Hasson, U., Nir, Y., Levy, I., Fuhrmann, G., Malach, R., 2004. Intersubject synchronization of cortical activity during natural vision. Science 303 (5664), 1634–1640. https://doi.org/10.1126/science.1089506.

Hasson, U., Yang, E., Vallines, I., Heeger, D.J., Rubin, N., 2008. A hierarchy of temporal receptive windows in human cortex. J. Neurosci. 28 (10), 2539–2550. https://doi.org/10.1523/JNEUROSCI.5487-07.2008.

Hawrylycz, M.J., Lein, E.S., Guillozet-Bongaarts, A.L., Shen, E.H., Ng, L., Miller, J.A., van de Lagemaat, L.N., Smith, K.A., Ebbert, A., Riley, Z.L., Abajian, C., Beckmann, C.F., Bernard, A., Bertagnolli, D., Boe, A.F., Cartagena, P.M., Chakravarty, M.M., Chapin, M., Chong, J., Jones, A.R., 2012. An anatomically comprehensive atlas of the adult human brain transcriptome. Nature 489 (7416), 391–399. https://doi.org/10.1038/nature11405.

Hollenbach, F.M., Montgomery, J.M., 2020. Bayesian Model Selection, Model Comparison, and Model Averaging. The SAGE Handbook of Research Methods in Political Science and International Relations, pp. 937–960. https://doi.org/10.4135/9781526486387.n52.

Honey, C.J., Thesen, T., Donner, T.H., Silbert, L.J., Carlson, C.E., Devinsky, O., Doyle, W.K., Rubin, N., Heeger, D.J., Hasson, U., 2012. Slow cortical dynamics and the accumulation of information over long timescales. Neuron 76 (2), 423–434. https://doi.org/10.1016/j.neuron.2012.08.011.

Horn, A. (2016). *HCP-MMP1.0 projected on MNI2009a GM (volumetric) in NIfTI format.* https://doi.org/10.6084/m9.figshare.3501911.v5.

Huntenburg, J.M., Bazin, P.L., Goulas, A., Tardif, C.L., Villringer, A., Margulies, D.S., 2017. A systematic relationship between functional connectivity and intracortical myelin in the human cerebral cortex. Cereb. Cortex (New York, NY: 1991) 27 (2), 981–997. https://doi.org/10.1093/cercor/bhx030.

Huntenburg, J.M., Bazin, P.L., Margulies, D.S., 2018. Large-scale gradients in human cortical organization. Trends. Cogn. Sci. 22 (1), 21–31. https://doi.org/10.1016/j.tics.2017.11.002.

Ingvar, D.H., 1985. ``Memory of the future'': an essay on the temporal organization of conscious awareness. Hum. Neurobiol. 4 (3), 127–136.

Ito, T., Hearne, L.J., Cole, M.W., 2020. A cortical hierarchy of localized and distributed processes revealed via dissociation of task activations, connectivity changes, and intrinsic timescales. Neuroimage 221 (February), 117141. https://doi.org/10.1016/j.neuroimage.2020.117141.

Jääskeläinen, I.P., Sams, M., Glerean, E., Ahveninen, J., 2021. Movies and narratives as naturalistic stimuli in neuroimaging. Neuroimage 224 (June 2020), 117445. https://doi.org/10.1016/j.neuroimage.2020.117445.

Jenkinson, M., Bannister, P., Brady, M., Smith, S., 2002. Improved optimization for the robust and accurate linear registration and motion correction of brain images. Neuroimage 17 (2), 825–841. https://doi.org/10.1006/nimg.2002.1132.

Jenkinson, M., Beckmann, C.F., Behrens, T.E.J., Woolrich, M.W., Smith, S.M., 2012. FSL. Neuroimage 62 (2), 782–790. https://doi.org/10.1016/j.neuroimage.2011.09.015.

Jeon, H.A., 2014. Hierarchical processing in the prefrontal cortex in a variety of cognitive domains. Front. Syst. Neurosci. 8 (NOV), 1–8. https://doi.org/10.3389/fnsys.2014.00223. Frontiers Research Foundation.

Ji, J.L., Spronk, M., Kulkarni, K., Repovš, G., Anticevic, A., Cole, M.W., 2019. Mapping the human brain's cortical-subcortical functional network organization. Neuroimage 185 (October 2018), 35–57. https://doi.org/10.1016/j.neuroimage.2018.10.006.

Jobson, D.D., Hase, Y., Clarkson, A.N., Kalaria, R.N., 2021. The role of the medial prefrontal cortex in cognition, ageing and dementia. Brain Commun. 3 (3). https://doi.org/10.1093/braincomms/fcab125.

Jones, D.K., Knösche, T.R., Turner, R., 2013. White matter integrity, fiber count, and other fallacies: the do's and don'ts of diffusion MRI. Neuroimage 73, 239–254. https://doi.org/10.1016/j.neuroimage.2012.06.081.

Jung, J.Y., Cloutman, L.L., Binney, R.J., Lambon Ralph, M.A., 2017. The structural connectivity of higher order association cortices reflects human functional brain networks. Cortex 97, 221–239. https://doi.org/10.1016/j.cortex.2016.08.011.

Kai, J., Khan, A.R., Haast, R.A., Lau, J.C., 2022. Mapping the subcortical connectome using in vivo diffusion MRI: feasibility and reliability. Neuroimage 262 (March), 119553. https://doi.org/10.1016/j.neuroimage.2022.119553.

Keller, A.S., Sydnor, V.J., Pines, A., Fair, D.A., Bassett, D.S., Satterthwaite, T.D., 2023. Hierarchical functional system development supports executive function. Trends. Cogn. Sci. 27 (2), 160–174. https://doi.org/10.1016/j.tics.2022.11.005.

Kiebel, S.J., Daunizeau, J., Friston, K.J., 2008. A hierarchy of time-scales and the brain. PLoS Comput. Biol. 4 (11). https://doi.org/10.1371/journal.pcbi.1000209.

Koechlin, E., Summerfield, C., 2007. An information theoretical approach to prefrontal executive function. Trends Cogn. Sci. 11 (6), 229–235. https://doi.org/10.1016/j.tics.2007.04.005.

Kruschke, J.K., 2011. Tutorial: doing Bayesian data analysis with R and BUGS. In: Expanding the Space of Cognitive Science - Proceedings of the 33rd Annual Meeting of the Cognitive Science Society, CogSci 2011, pp. 56–57.

Lee, D.K., 2016. Alternatives to P value: confidence interval and effect size. Korean J. Anesthesiol. 69 (6), 555. https://doi.org/10.4097/kjae.2016.69.6.555.

Lerner, Y., Honey, C.J., Silbert, L.J., Hasson, U., 2011. Topographic mapping of a hierarchy of temporal receptive windows using a narrated story. J. Neurosci. 31 (8), 2906–2915. https://doi.org/10.1523/JNEUROSCI.3684-10.2011.

Liu, Z.Q., Shafiei, G., Baillet, S., Misic, B., 2023. Spatially heterogeneous structure-function coupling in haemodynamic and electromagnetic brain networks. Neuroimage 278 (July), 120276. https://doi.org/10.1016/j.neuroimage.2023.120276.

Lohia, K., Soans, R.S., Saxena, R., Mahajan, K., Gandhi, T.K., 2024. Distinct rich and diverse clubs regulate coarse and fine binocular disparity processing: evidence from stereoscopic task-based fMRI. iScience, 109831. https://doi.org/10.1016/j.isci.2024.109831.

Lurie, D.J., Pappas, I., D'Esposito, M, 2024. Cortical timescales and the modular organization of structural and functional brain networks. Hum. Brain Mapp. 45 (2). https://doi.org/10.1002/hbm.26587.

Mahjoory, K., Schoffelen, J.M., Keitel, A., Gross, J., 2020. The frequency gradient of human resting-state brain oscillations follows cortical hierarchies. Elife 9, 1–18. https://doi.org/10.7554/ELIFE.53715.

Maldjian, J.A., Laurienti, P.J., Kraft, R.A., Burdette, J.H., 2003. An automated method for neuroanatomic and cytoarchitectonic atlas-based interrogation of fMRI data sets. Neuroimage 19 (3), 1233–1239. https://doi.org/10.1016/S1053-8119(03)00169-1.

Manea, A.M.G., Zilverstand, A., Ugurbil, K., Heilbronner, S.R., Zimmermann, J., 2022. Intrinsic timescales as an organizational principle of neural processing across the whole rhesus macaque brain. Elife 11, 1–20. https://doi.org/10.7554/eLife.75540.

Margulies, D.S., Ghosh, S.S., Goulas, A., Falkiewicz, M., Huntenburg, J.M., Langs, G., Bezgin, G., Eickhoff, S.B., Castellanos, F.X., Petrides, M., Jefferies, E., Smallwood, J., 2016. Situating the default-mode network along a principal gradient of macroscale cortical organization. Proc. Natl. Acad. Sci. USA 113 (44), 12574–12579. https://doi.org/10.1073/pnas.1608282113.

Markello, R.D., Hansen, J.Y., Liu, Z.Q., Bazinet, V., Shafiei, G., Suárez, L.E., Blostein, N., Seidlitz, J., Baillet, S., Satterthwaite, T.D., Chakravarty, M.M., Raznahan, A., Misic, B., 2022. Neuromaps: structural and functional interpretation of brain maps. Nat. Methods 19 (11), 1472–1479. https://doi.org/10.1038/s41592-022-01625-w.

Mashour, G.A., Roelfsema, P., Changeux, J.P., Dehaene, S., 2020. Conscious processing and the global neuronal workspace hypothesis. Neuron 105 (5), 776–798. https://doi.org/10.1016/j.neuron.2020.01.026.

Mathy, F., Feldman, J., 2012. What's magic about magic numbers? Chunking and data compression in short-term memory. Cognition 122 (3), 346–362. https://doi.org/10.1016/j.cognition.2011.11.003.

Mecklenbrauck, F., Gruber, M., Siestrup, S., Zahedi, A., Grotegerd, D., Mauritz, M., Trempler, I., Dannlowski, U., Schubotz, R.I., 2024. The significance of structural rich club hubs for the processing of hierarchical stimuli. Hum. Brain Mapp. 45 (4), 1–28. https://doi.org/10.1002/hbm.26543.

Meilă, M., 2003. Comparing clusterings by the variation of information. In: Lecture Notes in Artificial Intelligence (Subseries of Lecture Notes in Computer Science), 2777, pp. 173–187. https://doi.org/10.1007/978-3-540-45167-9_14.

Mesulam, M.M., 1998. From sensation to cognition. Brain 121 (6), 1013–1052. https://doi.org/10.1093/brain/121.6.1013.

Mohor, G.S., Thieken, A.H., Korup, O., 2021. Residential flood loss estimated from Bayesian multilevel models. Nat. Haz. Earth Syst. Sci. 21 (5), 1599–1614. https://doi.org/10.5194/nhess-21-1599-2021.

Moraczewski, D., Nketia, J., Redcay, E., 2020. Cortical temporal hierarchy is immature in middle childhood. Neuroimage 216 (June 2019), 116616. https://doi.org/10.1016/j.neuroimage.2020.116616.

Mori, S., Crain, B.J., Chacko, V.P., van Zilj, P.C.M., 1999. Three-dimensional tracking of axonal projections in the brain by magnetic resonance imaging. Ann. Neurol. 45 (2), 265–269. https://doi.org/10.1002/1531-8249(199902)45:2<247::AID-ANA16>3.0.CO;2-U.

Müller, E.J., Munn, B., Hearne, L.J., Smith, J.B., Fulcher, B., Arnatkevičiūtė, A., Lurie, D. J., Cocchi, L., Shine, J.M., 2020. Core and matrix thalamic sub-populations relate to spatio-temporal cortical connectivity gradients. Neuroimage 222 (August), 117224. https://doi.org/10.1016/j.neuroimage.2020.117224.

Murphy, C., Wang, H.T., Konu, D., Lowndes, R., Margulies, D.S., Jefferies, E., Smallwood, J., 2019. Modes of operation: a topographic neural gradient supporting stimulus dependent and independent cognition. Neuroimage 186 (November 2018), 487–496. https://doi.org/10.1016/j.neuroimage.2018.11.009.

Murray, J.D., Bernacchia, A., Freedman, D.J., Romo, R., Wallis, J.D., Cai, X., Padoa-Schioppa, C., Pasternak, T., Seo, H., Lee, D., Wang, X.J., 2014. A hierarchy of intrinsic timescales across primate cortex. Nat. Neurosci. 17 (12), 1661–1663. https://doi.org/10.1038/nn.3862.

Nastase, S.A., Gazzola, V., Hasson, U., Keysers, C., 2019. Measuring shared responses across subjects using intersubject correlation. Soc. Cogn. Affect. Neurosci. 14 (6), 669–687. https://doi.org/10.1093/scan/nsz037.

Neudorf, J., Ekstrand, C., Kress, S., Borowsky, R., 2020. Brain structural connectivity predicts brain functional complexity: diffusion tensor imaging derived centrality accounts for variance in fractal properties of functional magnetic resonance imaging signal. Neuroscience 438, 1–8. https://doi.org/10.1016/j.neuroscience.2020.04.048.

Nieder, A., 2016. Representing something out of nothing: the dawning of zero. Trends Cogn. Sci. 20 (11), 830–842. https://doi.org/10.1016/j.tics.2016.08.008.

Ogawa, T., Komatsu, H., 2010. Differential temporal storage capacity in the baseline activity of neurons in macaque frontal eye field and area V4. J. Neurophysiol. 103 (5), 2433–2445. https://doi.org/10.1152/jn.01066.2009.

Oldfield, R.C., 1971. The assessment and analysis of handedness: the Edinburgh inventory. Neuropsychologia1 9, 97–113. https://doi.org/10.1007/978-3-319-55065-7_301010.

Oldham, S., Fornito, A., 2023. Hubs and rich clubs. Connectome Analysis: Characterization, Methods, and Analysis. INC. https://doi.org/10.1016/B978-0-323-85280-7.00015-4.

Oldham, S., Fulcher, B., Parkes, L., Arnatkeviciūtė, A., Suo, C., Fornito, A., 2019. Consistency and differences between centrality measures across distinct classes of networks. PLoS One 14 (7), 1–23. https://doi.org/10.1371/journal.pone.0220061.

Ortiz-Terán, L., Diez, I., Ortiz, T., Perez, D.L., Aragón, J.I., Costumero, V., Pascual-Leone, A., El Fakhri, G., Sepulcre, J, 2017. Brain circuit-gene expression relationships and neuroplasticity of multisensory cortices in blind children. Proc. Natl. Acad. Sci. USA 114 (26), 6830–6835. https://doi.org/10.1073/pnas.1619121114.

Patriat, R., Molloy, E.K., Meier, T.B., Kirk, G.R., Nair, V.A., Meyerand, M.E., Prabhakaran, V., Birn, R.M., 2013. The effect of resting condition on resting-state fMRI reliability and consistency: a comparison between resting with eyes open, closed, and fixated. Neuroimage 78, 463–473. https://doi.org/10.1016/j.neuroimage.2013.04.013.

Pinhas, M., Tzelgov, J., 2012. Expanding on the mental number line: zero is perceived as the "smallest''. J. Exp. Psychol. 38 (5), 1187–1205. https://doi.org/10.1037/a0027390.

Power, J.D., Barnes, K.A., Snyder, A.Z., Schlaggar, B.L., Petersen, S.E., 2012. Spurious but systematic correlations in functional connectivity MRI networks arise from subject motion. Neuroimage 59 (3), 2142–2154. https://doi.org/10.1016/j.neuroimage.2011.10.018.

Preti, M.G., Van De Ville, D., 2019. Decoupling of brain function from structure reveals regional behavioral specialization in humans. Nat. Commun. 10 (1), 1–7. https://doi.org/10.1038/s41467-019-12765-7.

Pretus, C., Marcos-Vidal, L., Martínez-García, M., Picado, M., Ramos-Quiroga, J.A., Richarte, V., Castellanos, F.X., Sepulcre, J., Desco, M., Vilarroya, Ó., Carmona, S., 2019. Stepwise functional connectivity reveals altered sensory-multimodal integration in medication-naïve adults with attention deficit hyperactivity disorder. Hum. Brain Mapp. 40 (16), 4645–4656. https://doi.org/10.1002/hbm.24727.

Qi, S., Meesters, S., Nicolay, K., ter Haar Romeny, B.M., Ossenblok, P., 2015. The influence of construction methodology on structural brain network measures: a review. J. Neurosci. Methods 253 (500), 170–182. https://doi.org/10.1016/j.jneumeth.2015.06.016.

R Core Team. (2022). *R: A Language and Environment for Statistical Computing.* https://www.r-project.org/.

Raut, R.V., Snyder, A.Z., Raichle, M.E., 2020. Hierarchical dynamics as a macroscopic organizing principle of the human brain. Proc. Natl. Acad. Sci. USA 117 (34), 20890–20897. https://doi.org/10.1073/pnas.2003383117.

Redcay, E., Moraczewski, D., 2020. Social cognition in context: a naturalistic imaging approach. Neuroimage 216 (October 2019), 116392. https://doi.org/10.1016/j.neuroimage.2019.116392.

Ren, Y., Nguyen, V.T., Guo, L., Guo, C.C., 2017. Inter-subject functional correlation reveal a hierarchical organization of extrinsic and intrinsic systems in the brain. Sci. Rep. 7 (1), 1–12. https://doi.org/10.1038/s41598-017-11324-8.

Riedel, L., van den Heuvel, M.P., Markett, S., 2022. Trajectory of rich club properties in structural brain networks. Hum. Brain Mapp. 43 (14), 4239–4253. https://doi.org/10.1002/hbm.25950.

Rouder, J.N., Haaf, J.M., Aust, F., 2018. From theories to models to predictions: a Bayesian model comparison approach. Commun. Monogr. 85 (1), 41–56. https://doi.org/10.1080/03637751.2017.1394581.

RStudio Team. (2022). *RStudio: Integrated Development Environment for R.* http://www.rstudio.com/.

Rubinov, M., Sporns, O., 2010. Complex network measures of brain connectivity: uses and interpretations. Neuroimage 52 (3), 1059–1069. https://doi.org/10.1016/j.neuroimage.2009.10.003.

Rust, N.C., Movshon, J.A., 2005. In praise of artifice. Nat. Neurosci. 8 (12), 1647–1650. https://doi.org/10.1038/nn1606.

Saberi, A., Paquola, C., Wagstyl, K., Hettwer, M.D., Bernhardt, B.C., Eickhoff, S.B., Valk, S.L., 2023. The regional variation of laminar thickness in the human isocortex is related to cortical hierarchy and interregional connectivity. PLoS Biol. 21 (11 November), 1–29. https://doi.org/10.1371/journal.pbio.3002365.

Satterthwaite, T.D., Elliott, M.A., Gerraty, R.T., Ruparel, K., Loughead, J., Calkins, M.E., Eickhoff, S.B., Hakonarson, H., Gur, R.C., Gur, R.E., Wolf, D.H., 2013. An improved framework for confound regression and filtering for control of motion artifact in the preprocessing of resting-state functional connectivity data. Neuroimage 64 (1), 240–256. https://doi.org/10.1016/j.neuroimage.2012.08.052.

Schaefer, A., Kong, R., Gordon, E.M., Laumann, T.O., Zuo, X.-N., Holmes, A.J., Eickhoff, S.B., Yeo, B.T.T., 2018. Local-global parcellation of the human cerebral cortex from intrinsic functional connectivity MRI. Cereb. Cortex 28 (9), 3095–3114. https://doi.org/10.1093/cercor/bhx179.

Schmälzle, R., Imhof, M.A., Grall, C., Flaisch, T., Schupp, H.T., Schmälzle, R., Imhof, M. A., Grall, C., Flaisch, T., & Schupp, H.T. (2017). Reliability of fMRI time series: similarity of neural processing during movie viewing. bioRxiv, 158188. https://doi.org/10.1101/158188.

Schmidt, M., Bakker, R., Shen, K., Bezgin, G., Diesmann, M., Van Albada, S.J., & Schmidt, M. (2016). *Full-density multi-scale account of structure and dynamics of macaque visual cortex correspondence to:* https://doi.org/10.48550/arXiv.1511.09364.

Scholtens, L.H., Schmidt, R., de Reus, M.A., van den Heuvel, M.P., 2014. Linking macroscale graph analytical organization to microscale neuroarchitectonics in the macaque connectome. J. Neurosci. 34 (36), 12192–12205. https://doi.org/10.1523/JNEUROSCI.0752-14.2014.

Seguin, C., Tian, Y., Zalesky, A., 2020. Network communication models improve the behavioral and functional predictive utility of the human structural connectome. Netw. Neurosci. 4 (4), 980–1006. https://doi.org/10.1162/netn_a_00161.

Senden, M., Deco, G., De Reus, M.A., Goebel, R., van den Heuvel, M.P., 2014. Rich club organization supports a diverse set of functional network configurations. Neuroimage 96, 174–182. https://doi.org/10.1016/j.neuroimage.2014.03.066.

Senden, M., Reuter, N., van den Heuvel, M.P., Goebel, R., Deco, G., 2017. Cortical rich club regions can organize state-dependent functional network formation by engaging in oscillatory behavior. Neuroimage 146, 561–574. https://doi.org/10.1016/j.neuroimage.2016.10.044.

Sepulcre, J., 2014. Integration of visual and motor functional streams in the human brain. Neurosci. Lett. 567, 68–73. https://doi.org/10.1016/j.neulet.2014.03.050.

Sepulcre, J., Liu, H., Talukdar, T., Martincorena, I., Thomas Yeo, B.T., Buckner, R.L., 2010. The organization of local and distant functional connectivity in the human brain. PLoS Comput. Biol. 6 (6), 1–15. https://doi.org/10.1371/journal.pcbi.1000808.

Sepulcre, J., Sabuncu, M.R., Yeo, T.B., Liu, H., Johnson, K.A., 2012. Stepwise connectivity of the modal cortex reveals the multimodal organization of the human brain. J. Neurosci. 32 (31), 10649–10661. https://doi.org/10.1523/JNEUROSCI.0759-12.2012.

Sethi, S.S., Zerbi, V., Wenderoth, N., Fornito, A., Fulcher, B.D., 2017. Structural connectome topology relates to regional BOLD signal dynamics in the mouse brain. Chaos 27 (4). https://doi.org/10.1063/1.4979281.

Shafiei, G., Fulcher, B.D., Voytek, B., Satterthwaite, T.D., Baillet, S., Misic, B., 2023. Neurophysiological signatures of cortical micro-architecture. Nat. Commun. 14 (1). https://doi.org/10.1038/s41467-023-41689-6.

Shafiei, G., Markello, R.D., De Wael, R.V., Bernhardt, B.C., Fulcher, B.D., Misic, B., 2020. Topographic gradients of intrinsic dynamics across neocortex. Elife 9, 1–24. https://doi.org/10.7554/eLife.62116.

Shen, X., Tokoglu, F., Papademetris, X., Constable, R.T., 2013. Groupwise whole-brain parcellation from resting-state fMRI data for network node identification. Neuroimage 82, 403–415. https://doi.org/10.1016/j.neuroimage.2013.05.081.

Shine, J.M., Hearne, L.J., Breakspear, M., Hwang, K., Müller, E.J., Sporns, O., Poldrack, R.A., Mattingley, J.B., Cocchi, L., 2019. The low-dimensional neural architecture of cognitive complexity is related to activity in medial thalamic nuclei. Neuron 104 (5), 849–855.e3. https://doi.org/10.1016/j.neuron.2019.09.002.

Siegle, J.H., Jia, X., Durand, S., Gale, S., Bennett, C., Graddis, N., Heller, G., Ramirez, T. K., Choi, H., Luviano, J.A., Groblewski, P.A., Ahmed, R., Arkhipov, A., Bernard, A., Billeh, Y.N., Brown, D., Buice, M.A., Cain, N., Caldejon, S., Koch, C., 2021. Survey of spiking in the mouse visual system reveals functional hierarchy. Nature 592 (7852), 86–92. https://doi.org/10.1038/s41586-020-03171-x.

Smith, S.M., Jenkinson, M., Woolrich, M.W., Beckmann, C.F., Behrens, T.E.J., Johansen-Berg, H., Bannister, P.R., De Luca, M., Drobnjak, I., Flitney, D.E., Niazy, R.K., Saunders, J., Vickers, J., Zhang, Y., De Stefano, N., Brady, J.M., Matthews, P.M., 2004. Advances in functional and structural MR image analysis and implementation as FSL. Neuroimage 23 (SUPPL. 1), 208–219. https://doi.org/10.1016/j.neuroimage.2004.07.051.

Soltani, A., Murray, J.D., Seo, H., Lee, D., 2021. Timescales of cognition in the brain. Curr. Opin. Behav. Sci. 41, 30–37. https://doi.org/10.1016/j.cobeha.2021.03.003.

Sonkusare, S., Breakspear, M., Guo, C., 2019. Naturalistic stimuli in neuroscience: critically acclaimed. Trends. Cogn. Sci. 23 (8), 699–714. https://doi.org/10.1016/j.tics.2019.05.004.

Sporns, O., 2011. The human connectome: a complex network. Ann. N. Y. Acad. Sci. 1224 (1), 109–125. https://doi.org/10.1111/j.1749-6632.2010.05888.x.

Stephens, G.J., Honey, C.J., Hasson, U., 2013. A place for time: the spatiotemporal structure of neural dynamics during natural audition. J. Neurophysiol. 110 (9), 2019–2026. https://doi.org/10.1152/jn.00268.2013.

Sydnor, V.J., Larsen, B., Bassett, D.S., Alexander-Bloch, A., Fair, D.A., Liston, C., Mackey, A.P., Milham, M.P., Pines, A., Roalf, D.R., Seidlitz, J., Xu, T., Raznahan, A., Satterthwaite, T.D., 2021. Neurodevelopment of the association cortices: patterns, mechanisms, and implications for psychopathology. Neuron 109 (18), 2820–2846. https://doi.org/10.1016/j.neuron.2021.06.016.

Sydnor, V.J., Larsen, B., Seidlitz, J., Adebimpe, A., Alexander-Bloch, A.F., Bassett, D.S., Bertolero, M.A., Cieslak, M., Covitz, S., Fan, Y., Gur, R.E., Gur, R.C., Mackey, A.P., Moore, T.M., Roalf, D.R., Shinohara, R.T., Satterthwaite, T.D., 2023. Intrinsic activity development unfolds along a sensorimotor–association cortical axis in youth. Nat. Neurosci. 26 (4), 638–649. https://doi.org/10.1038/s41593-023-01282-y.

Taylor, P., Hobbs, J.N., Burroni, J., Siegelmann, H.T., 2015. The global landscape of cognition: hierarchical aggregation as an organizational principle of human cortical networks and functions. Sci. Rep. 5 (November), 1–18. https://doi.org/10.1038/srep18112.

The MathWorks Inc., 2021. MATLAB version: 9.10.0 (R2021a). The MathWorks Inc. https://www.mathworks.com.

Thomas, R.M., De Sanctis, T., Gazzola, V., Keysers, C., 2018. Where and how our brain represents the temporal structure of observed action. Neuroimage 183 (November 2017), 677–697. https://doi.org/10.1016/j.neuroimage.2018.08.056.

Tomczak, M., Tomczak, E., 2014. The need to report effect size estimates revisited. An overview of some recommended measures of effect size. Trends Sport Sci. 1 (21), 19–25. http://www.wbc.poznan.pl/Content/325867/5_Trends_Vol21_2014_no1_20.pdf.

Torres-Gomez, S., Blonde, J.D., Mendoza-Halliday, D., Kuebler, E., Everest, M., Wang, X.-J., Inoue, W., Poulter, M.O., Martinez-Trujillo, J., 2020. Changes in the proportion of inhibitory interneuron types from sensory to executive areas of the primate neocortex: implications for the origins of working memory representations. Cereb. Cortex 30 (8), 4544–4562. https://doi.org/10.1093/cercor/bhaa056.

Tourbier, S., Aleman-Gomez, Y., Griffa, A., Bach Cuadra, M., & Hagmann, P. (2019). *Sebastientourbier/multiscalebrainparcellator: Multi-Scale Brain Parcellator v1.1.1.* https://doi.org/10.5281/ZENODO.3627097.

Tzourio-Mazoyer, N., Landeau, B., Papathanassiou, D., Crivello, F., Etard, O., Delcroix, N., Mazoyer, B., Joliot, M., 2002. Automated anatomical labeling of activations in SPM using a macroscopic anatomical parcellation of the MNI MRI single-subject brain. Neuroimage 15 (1), 273–289. https://doi.org/10.1006/nimg.2001.0978.

Uithol, S., van Rooij, I., Bekkering, H., Haselager, P., 2012. Hierarchies in action and motor control. J. Cogn. Neurosci. 24 (5), 1077–1086. https://doi.org/10.1162/jocn_a_00204.

Valk, S.L., Xu, T., Margulies, D.S., Masouleh, S.K., Paquola, C., Goulas, A., Kochunov, P., Smallwood, J., Yeo, B.T.T., Bernhardt, B.C., Eickhoff, S.B., 2020. Shaping brain structure: genetic and phylogenetic axes of macroscale organization of cortical thickness. Sci. Adv. 6 (39), 1–14. https://doi.org/10.1126/sciadv.abb3417.

van den Heuvel, M.P., Scholtens, L.H., Barrett, L.F., Hilgetag, C.C., de Reus, M.A., 2015. Bridging cytoarchitectonics and connectomics in human cerebral cortex. J. Neurosci. 35 (41), 13943–13948. https://doi.org/10.1523/JNEUROSCI.2630-15.2015.

van den Heuvel, M.P., Scholtens, L.H., van der Burgh, H.K., Agosta, F., Alloza, C., Arango, C., Auyeung, B., Baron-Cohen, S., Basaia, S., Benders, M.J.N.L., Beyer, F., Booij, L., Braun, K.P.J., Filho, G.B., Cahn, W., Cannon, D.M., Chaim-Avancini, T.M., Chan, S.S.M., Chen, E.Y.H., de Lange, S.C., 2019. 10kin1day: a bottom-up neuroimaging initiative. Front. Neurol. 10 (MAY). https://doi.org/10.3389/fneur.2019.00425.

van den Heuvel, M.P., Sporns, O., 2011. Rich-club organization of the human connectome. J. Neurosci. 31 (44), 15775–15786. https://doi.org/10.1523/JNEUROSCI.3539-11.2011.

van den Heuvel, M.P., Sporns, O., 2013a. An anatomical substrate for integration among functional networks in human cortex. J. Neurosci. 33 (36), 14489–14500. https://doi.org/10.1523/JNEUROSCI.2128-13.2013.

van den Heuvel, M.P., Sporns, O., 2013b. Network hubs in the human brain. Trends Cogn. Sci. 17 (12), 683–696. https://doi.org/10.1016/j.tics.2013.09.012.

van den Heuvel, M.P., Sporns, O., Collin, G., Scheewe, T., Mandl, R.C.W., Cahn, W., Goni, J., Pol, H.E.H., Kahn, R.S., 2013. Abnormal rich club organization and functional brain dynamics in schizophrenia. JAMA Psychiatry 70 (8), 783–792. https://doi.org/10.1001/jamapsychiatry.2013.1328.

Van Dijk, K.R.A., Hedden, T., Venkataraman, A., Evans, K.C., Lazar, S.W., Buckner, R.L., 2010. Intrinsic functional connectivity as a tool for human connectomics: theory, properties, and optimization. J. Neurophysiol. 103 (1), 297–321. https://doi.org/10.1152/jn.00783.2009.

van Doorn, J., van den Bergh, D., Böhm, U., Dablander, F., Derks, K., Draws, T., Etz, A., Evans, N.J., Gronau, Q.F., Haaf, J.M., Hinne, M., Kucharský, Š., Ly, A., Marsman, M., Matzke, D., Gupta, A.R.K.N., Sarafoglou, A., Stefan, A., Voelkel, J.G., Wagenmakers, E.J., 2021. The JASP guidelines for conducting and reporting a Bayesian analysis. Psychon. Bull. Rev. 28 (3), 813–826. https://doi.org/10.3758/s13423-020-01798-5.

Vázquez-Rodríguez, B., Suárez, L.E., Markello, R.D., Shafiei, G., Paquola, C., Hagmann, P., Van Den Heuvel, M.P., Bernhardt, B.C., Spreng, R.N., Misic, B, 2019. Gradients of structure–function tethering across neocortex. Proc. Natl. Acad. Sci. USA 116 (42), 21219–21227. https://doi.org/10.1073/pnas.1903403116.

Vehtari, A., 2024. Loo Package Glossary - Loo-Glossary. Loo-Glossary • Loo. https://mc-stan.org/loo/reference/loo-glossary.html.

Vehtari, A., Gelman, A., Gabry, J., 2017. Practical Bayesian model evaluation using leave-one-out cross-validation and WAIC. Stat. Comput. 27 (5), 1413–1432. https://doi.org/10.1007/s11222-016-9696-4.

Vehtari, A., Gelman, A., Simpson, D., Carpenter, B., Bürkner, P.-C., 2021. Rank-normalization, folding, and localization: an improved $\hat{R}$ for assessing convergence of MCMC (with discussion). Bayesian Anal. 16 (2), 667–718. https://doi.org/10.1214/20-BA1221.

Vogelbacher, C., Möbius, T.W.D., Sommer, J., Schuster, V., Dannlowski, U., Kircher, T., Dempfle, A., Jansen, A., Bopp, M.H.A., 2018. The Marburg-Münster affective disorders cohort study (MACS): a quality assurance protocol for MR neuroimaging data. Neuroimage 172 (December 2017), 450–460. https://doi.org/10.1016/j.neuroimage.2018.01.079.

Wagstyl, K., Ronan, L., Goodyer, I.M., Fletcher, P.C., 2015. Cortical thickness gradients in structural hierarchies. Neuroimage 111, 241–250. https://doi.org/10.1016/j.neuroimage.2015.02.036.

Wang, M., Yang, Y., Wang, C., Gamo, N.J., Jin, L.E., Mazer, J.A., Morrison, J.H., Wang, X., Arnsten, A.F.T., 2012. Article NMDA receptors subserve persistent neuronal firing during working memory in dorsolateral prefrontal cortex. Neuron 77 (4), 736–749. https://doi.org/10.1016/j.neuron.2012.12.032.

Wang, X.-J., 2001. Synaptic reverberation underlying mnemonic persistent activity. Trends Neurosci. 24 (8), 455–463. https://doi.org/10.1016/S0166-2236(00)01868-3.

Wang, X.-J., 2020. Macroscopic gradients of synaptic excitation and inhibition in the neocortex. Nat. Rev. Neurosci. 21 (3), 169–178. https://doi.org/10.1038/s41583-020-0262-x.

Watanabe, T., 2013. Rich-club network topology to minimize synchronization cost due to phase difference among frequency-synchronized oscillators. Physica A 392 (5), 1246–1255. https://doi.org/10.1016/j.physa.2012.11.041.

Whitaker, K.J., Vértes, P.E., Romero-Garciaa, R., Váša, F., Moutoussis, M., Prabhu, G., Weiskopf, N., Callaghan, M.F., Wagstyl, K., Rittman, T., Tait, R., Ooi, C., Suckling, J., Inkster, B., Fonagy, P., Dolan, R.J., Jones, P.B., Goodyer, I.M., Bullmore, E.T., 2016. Adolescence is associated with genomically patterned consolidation of the hubs of the human brain connectome. Proc. Natl. Acad. Sci. USA 113 (32), 9105–9110. https://doi.org/10.1073/pnas.1601745113.

Wolff, A., Berberian, N., Golesorkhi, M., Gomez-Pilar, J., Zilio, F., Northoff, G., 2022. Intrinsic neural timescales: temporal integration and segregation. Trends Cogn. Sci. 26 (2), 159–173. https://doi.org/10.1016/j.tics.2021.11.007.

Wooldridge, J.M., 2013. Introductory Econometrics: A Modern Approach, fifth ed. South-Western Cengage Learning.

Xu, T., Nenning, K.H., Schwartz, E., Hong, S.J., Vogelstein, J.T., Goulas, A., Fair, D.A., Schroeder, C.E., Margulies, D.S., Smallwood, J., Milham, M.P., Langs, G., 2020. Cross-species functional alignment reveals evolutionary hierarchy within the connectome. Neuroimage 223 (September), 117346. https://doi.org/10.1016/j.neuroimage.2020.117346.

Xue, C., Sun, H., Hu, G., Qi, W., Yue, Y., Rao, J., Yang, W., Xiao, C., Chen, J., 2020. Disrupted patterns of rich-club and diverse-club organizations in subjective cognitive decline and amnestic mild cognitive impairment. Front. Neurosci. 14 (October), 1–14. https://doi.org/10.3389/fnins.2020.575652.

Yeh, F.C., Wedeen, V.J., Tseng, W.Y.I., 2010. Generalized q-sampling imaging. IEEE Trans. Med. ImAging 29 (9), 1626–1635. https://doi.org/10.1109/TMI.2010.2045126.

Yeo, B.T.T., Krienen, F.M., Eickhoff, S.B., Yaakub, S.N., Fox, P.T., Buckner, R.L., Asplund, C.L., Chee, M.W.L., 2015. Functional specialization and flexibility in human association cortex. Cereb. Cortex 25 (10), 3654–3672. https://doi.org/10.1093/cercor/bhu217.

Zamora-López, G., Chen, Y., Deco, G., Kringelbach, M.L., Zhou, C., 2016. Functional complexity emerging from anatomical constraints in the brain: the significance of network modularity and rich-clubs. Sci. Rep. 6 (November), 1–18. https://doi.org/10.1038/srep38424.

Zamora-López, G., Zhou, C., Kurths, J., 2009. Graph analysis of cortical networks reveals complex anatomical communication substrate. Chaos 19 (1). https://doi.org/10.1063/1.3089559.

Zamora-López, G., Zhou, C., Kurths, J., 2010. Cortical hubs form a module for multisensory integration on top of the hierarchy of cortical networks. Front. Neuroinform. 4 (MAR), 1–13. https://doi.org/10.3389/neuro.11.001.2010.

Zamora-López, G., Zhou, C., Kurths, J., 2011. Exploring brain function from anatomical connectivity. Front. Neurosci. 5 (JUN), 1–11. https://doi.org/10.3389/fnins.2011.00083.

Zilio, F., Gomez-Pilar, J., Cao, S., Zhang, J., Zang, D., Qi, Z., Tan, J., Hiromi, T., Wu, X., Fogel, S., Huang, Z., Hohmann, M.R., Fomina, T., Synofzik, M., Grosse-Wentrup, M., Owen, A.M., Northoff, G., 2021. Are intrinsic neural timescales related to sensory processing? Evidence from abnormal behavioral states. Neuroimage 226 (November 2020), 117579. https://doi.org/10.1016/j.neuroimage.2020.117579.